

# Photosensitive Ru(II) Complexes as Inhibitors of the Major Human Drug Metabolizing Enzyme CYP3A4

Nicholas Toupin,<sup>1</sup> Sean J. Steinke,<sup>2</sup> Sandeep Nadella,<sup>1</sup> Ao Li,<sup>1</sup> T. N. Rohrbaugh, Jr.,<sup>2</sup>

Eric R. Samuels,<sup>3#</sup> Claudia Turro,<sup>2,\*</sup> Irina F. Sevrioukova,<sup>4,\*</sup> and Jeremy J. Kodanko<sup>1,5,\*</sup>

<sup>1</sup>*Department of Chemistry, Wayne State University, 5101 Cass Ave, Detroit, MI 48202,*

<sup>2</sup>*Department of Chemistry and Biochemistry, The Ohio State University, Columbus, Ohio 43210,*

<sup>3</sup>*Departments of Pharmaceutical Sciences and <sup>4</sup>Molecular Biology and Biochemistry, University of California, Irvine, CA 92697*

<sup>5</sup>*Barbara Ann Karmanos Cancer Institute, Detroit, Michigan 48201*

#Present address: AbbVie Inc., Irvine, CA 92612

[\\*sevrioui@uci.edu](mailto:sevrioui@uci.edu), [turro@chemistry.ohio-state.edu](mailto:turro@chemistry.ohio-state.edu), [jkodanko@chem.wayne.edu](mailto:jkodanko@chem.wayne.edu)

**Abstract.** We report the synthesis and photochemical and biological characterization of the first selective and potent metal-based inhibitors of cytochrome P450 3A4 (CYP3A4), the major human drug metabolizing enzyme. Five Ru(II)-based derivatives were prepared from two analogs of the CYP3A4 inhibitor ritonavir, **4** and **6**: [Ru(tpy)(L)(**6**)]Cl<sub>2</sub> (tpy = 2,2':6',2"-terpyridine) with L = 6,6'-dimethyl-2,2'-bipyridine (Me<sub>2</sub>bpy; **8**), dimethylbenzo[i]dipyrido[3,2-a:2',3'-c]phenazine (Me<sub>2</sub>dppn; **10**) and 3,6-dimethyl-10,15-diphenylbenzo[i]dipyrido[3,2-a:2',3'-c]phenazine (Me<sub>2</sub>Ph<sub>2</sub>dppn; **11**), [Ru(tpy)(Me<sub>2</sub>bpy)(**4**)]Cl<sub>2</sub> (**7**) and [Ru(tpy)(Me<sub>2</sub>dppn)(**4**)]Cl<sub>2</sub> (**9**). Photochemical release of **4** or **6** from **7** – **11** was demonstrated and the spectrophotometric evaluation of **7** showed that it behaves similarly to free **4** (type II heme ligation) after irradiation with visible light but not in the dark. Unexpectedly, the intact Ru(II) complexes **7** and **8** were found to inhibit CYP3A4 potently and specifically through direct binding to the active site without heme ligation. Caged inhibitors **9** – **11** showed dual action properties by combining photoactivated dissociation of **4** or **6** with efficient <sup>1</sup>O<sub>2</sub> production. In the prostate adenocarcinoma DU-145 cells,

compound **9** had the best synergistic effect with vinblastine, the anti-cancer drug primarily metabolized by CYP3A4 *in vivo*. Thus, our study establishes a new paradigm in CYP inhibition by metallated complexes and suggests possible utilization of photoactive CYP3A4 inhibitory compounds in clinical applications, such as enhancement of therapeutic efficacy of anti-cancer drugs.

## Introduction

Cytochrome P450s (CYPs) are heme-containing enzymes that play a crucial role in biosynthesis and metabolism. In addition to their activity in the liver, CYPs perform biosynthetic processing and drug oxidation in many other tissues, including the gastrointestinal tract and the brain. Extrahepatic CYP activity reduces local drug bioavailability and fuels resistance and progression of diseases, such as cancer, making CYPs attractive drug targets. Better understanding of the CYP inhibitory mechanism can also help lower the risk of dangerous drug-drug interactions. Genetic diversity of human CYPs leads to pharmacokinetic differences between people of different ethnic backgrounds that make drug responses highly varied. As a result, thorough characterization of small molecule interactions with CYPs is essential; in combination with genetic sequencing, these data will one day lead to better designed and personalized therapies.<sup>1</sup>

CYP3A4 is the most abundant liver and intestinal P450 isoform that oxidizes the majority of administered drugs and other xenobiotics relevant to human health.<sup>2-9</sup> Fast and overly extensive drug metabolism can reduce treatment efficacy by requiring higher doses to achieve the full therapeutic effect. One way to overcome fast drug metabolism is the inhibition of CYP3A4. Currently, two CYP3A4 inhibitors, ritonavir and cobicistat, are part of multi-drug therapies for treating HIV and Hepatitis C virus (HCV) infections, whereas ketoconazole is co-prescribed with the quickly-metabolized immunosuppressants in organ transplant patients.<sup>10-14</sup> Anti-cancer therapy

is another field where targeted CYP3A4 inhibition holds promise. CYP3A4 clears various types of anticancer drugs via both the intestinal/hepatic metabolism and enhanced expression/*in situ* metabolism in solid tumors.<sup>15-19</sup> Targeted inhibition of CYP3A4 in tumors has been identified as a potential solution to improve efficacy of chemotherapy by restoring sensitivity of cancer cells.<sup>19-20</sup> Since most anticancer drugs have a narrow therapeutic index, potent CYP3A4 inhibition (as part of drug cocktails) has great potential to improve outcomes, lower chemotherapeutic doses, and minimize adverse effects. Importantly, clinicians have already identified an urgent need for localized CYP3A4 inhibition in malignant tissues.<sup>21</sup> Localized inhibition was postulated to be more effective than systemic inhibition in colorectal cancer because a widely prescribed class of chemotherapeutics that destabilize microtubules are metabolized by CYP3A4 in cancer cells but by other CYPs in the liver.<sup>21</sup> Importantly, there are no current methods that achieve tissue-specific blockade of CYP activity. Moreover, unlike the thousands of organic small molecules characterized as CYP inhibitors, inducers or substrates, only a small handful of metal complexes have been investigated for CYP targeting.<sup>22-24</sup>

With the potential benefits in mind, we identified photocaging as a viable strategy to achieve localized CYP inhibition. Photocaging is a powerful method for blocking the action of biologically active molecules and unleashing inhibitory compounds within desired tissues, through which highly controlled and localized CYP inhibition could be achieved.<sup>22-23</sup> Towards this goal, Ru(II)-based photocaging can facilitate small molecule release in a non-invasive manner to provide spatial and temporal control over biological activity.<sup>25-27</sup> Photocaging has been exploited in basic research and for drug activation during photochemotherapy (PCT),<sup>28-30</sup> with recent *in vivo* validation of Ru(II)-PCT.<sup>31</sup> In addition to PCT, Ru(II) complexes show attractive properties for photodynamic therapy (PDT) applications, including high stability and cell permeability,<sup>32-33</sup> low

inherent toxicity,<sup>34-37</sup> and higher light-to-dark ratios for cell death compared to clinically approved PDT compounds.<sup>29, 38</sup> Due to their rich photochemistry and resistance to photobleaching,<sup>39</sup> a common problem with current organic photosensitizers,<sup>40</sup> ruthenium complexes are emerging as a promising new class of PDT agents,<sup>29, 41-43</sup> some of which have advanced to clinical trials.<sup>44-47</sup> One recent example is the Ru(II) photosensitizer TLD-1433, which is currently in Phase II clinical trials for the treatment of bladder cancer.<sup>48-50</sup>

Many small molecules that target CYPs contain *N*-donor heterocycles that coordinate to the heme iron in the active site (type II ligation) to create strong and stable enzyme-inhibitor complexes.<sup>51-53</sup> Ru(II) photocaging is an effective strategy for blocking *N*-donor heterocycles from binding to their targets, including the hemes found in CYP enzymes. Strong and stable coordination between *N*-donors, such as imidazoyl and pyridyl groups, and the Ru(II) centers of the photocages.<sup>26</sup> Examples include the photochemical release of the CYP17A1 inhibitor abiraterone in PC3 prostate adenocarcinoma cancer cells,<sup>23</sup> CYP11B1 inhibitors metyrapone and etomidate caged with the Ru(bpy)<sub>2</sub> (bpy = 2,2'-bipyridine) fragment,<sup>22</sup> and photocaged analogs of the pan-P450 inhibitor econazole that function as photoactivated cytotoxic and emissive agents in DLD-1 colon adenocarcinoma cancer cells.<sup>24</sup>

Herein, we report the design, synthesis and biochemical characterization of a series of photocaged CYP3A4 inhibitors. Compounds were designed as Ru(II)-caged analogs of the antiretroviral drug ritonavir,<sup>54</sup> which is a CYP3A4 inhibitor that binds tightly to the heme iron center via its thiazole ring.<sup>51, 53</sup> Two types of Ru(II) photocaging groups were employed that show either single action PCT or dual action PCT/PDT behaviors. All compounds were highly stable in solution in the dark but released CYP3A4 inhibitors readily upon irradiation with visible light, enabling type II heme iron ligation. While the main goal of the project was to design and employ

light-activated CYP inhibitory molecules, one unexpected and significant finding was that, even without light activation, some Ru(II) compounds could potently inhibit CYP3A4 by binding to the active site without heme ligation. A direct inhibitory action between a large metal complex and a CYP target was verified by X-ray crystallography. Finally, we report that photocaged CYP3A4 inhibitors can function as dual action PDT and PCT agents that can both generate  ${}^1\text{O}_2$  and release the inhibitor upon irradiation, respectively. It is shown that these compounds work synergistically with the microtubule-destabilizing drug vinblastine, primarily metabolized by CYP3A4 *in vivo*. Thus, this work establishes a new paradigm in CYP inhibition and raises the possibility that photoactive CYP3A4 inhibitory compounds can be utilized in clinical applications, such as enhancement of therapeutic efficacy of anti-cancer drugs.

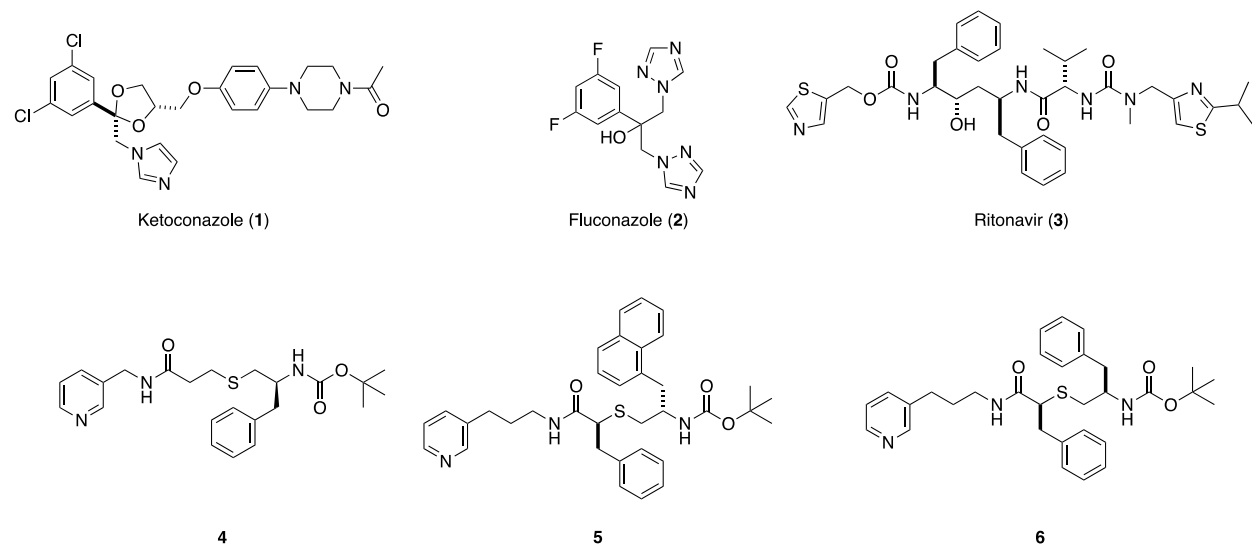
## Results and Discussion

### Compound Design and Synthesis

To begin our studies, we surveyed the literature for known type II inhibitors of CYP3A4. Clinical examples include ketoconazole (**1**), fluconazole (**2**) and ritonavir (**3**) that contain imidazole, triazole or thiazole *N*-donors, respectively (Figure 1).<sup>51, 55-56</sup> Instead, we chose to focus our efforts on CYP3A4 inhibitors containing pyridyl groups that are analogs of ritonavir (**4 – 6**).<sup>57-59</sup> Pyridine-containing compounds show more favorable properties for Ru(II) photocaging than other heterocyclic compounds, including strong and stable binding to Ru(II) in the dark and facile release when irradiated with low-energy light.<sup>23, 60-62</sup> Compounds **4 – 6** inhibit CYP3A4 in the low  $\mu\text{M}$  to nM range in *in vitro* assays with a fluorogenic substrate (*vide infra*) and, as verified by spectroscopic and X-ray crystallography analyses, inhibit CYP3A4 by ligating directly to the heme iron via the pyridine nitrogen.<sup>57-59</sup> Analogs **4** and **6** were chosen over **5**, which showed the lowest IC<sub>50</sub> value of the series (90 nM), but had the potential to create solubility problems in Ru(II)-caged complexes due to its hydrophobic nature. Compound **4** was obtained using a modified three-step

synthetic route that used trityl protection of 3-thiopropanoic acid (Scheme S1).<sup>57</sup> Compound **6** was synthesized from *S*-2-mercapto-3-phenylpropanoic acid<sup>63</sup> following a literature protocol.<sup>58</sup>

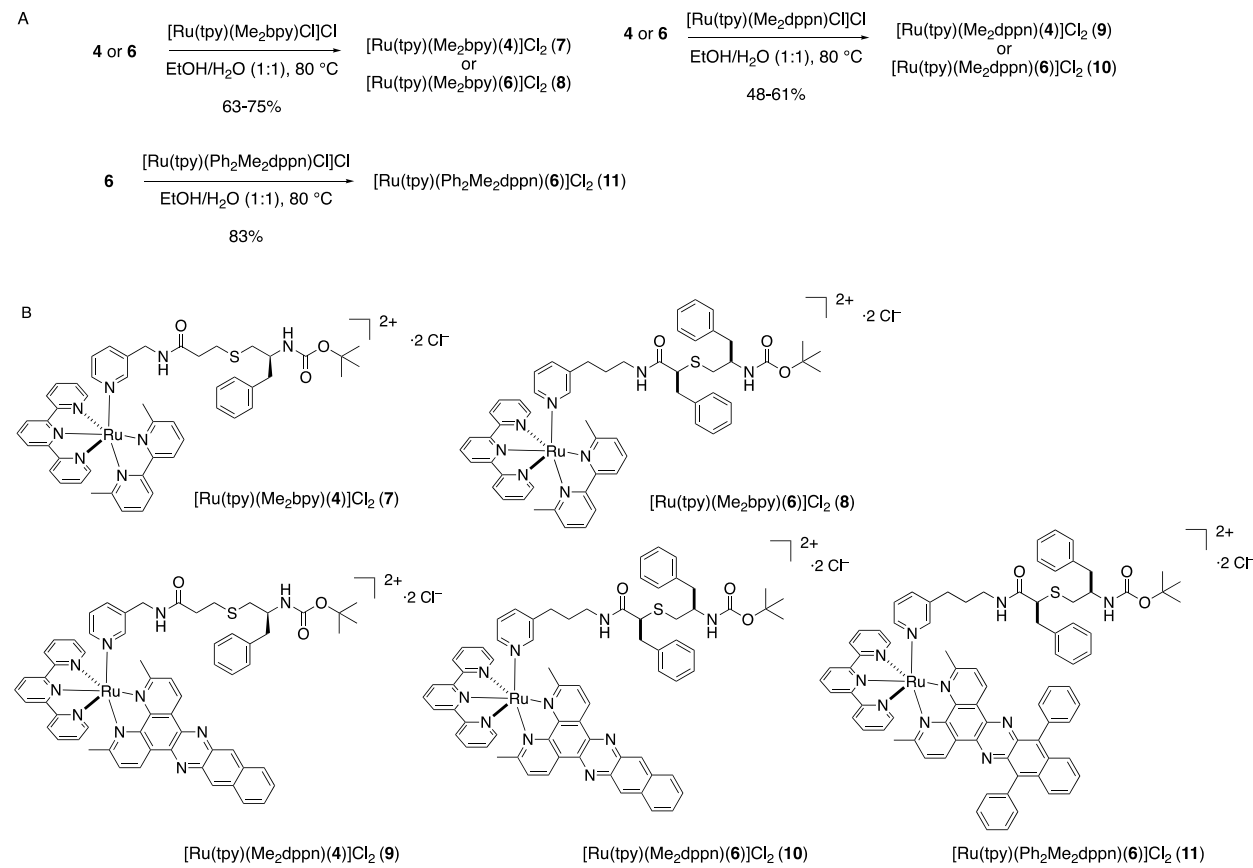
**Figure 1.** Structures of Type II CYP3A4 inhibitors including ritonavir and related analogs 4–6



Five Ru(II) complexes containing the caged analogs of CYP3A4 inhibitors **4** and **6** were prepared as shown in Scheme 1. Complexes **7** and **8**, coupled to the [Ru(tpy)(Me<sub>2</sub>bpy)] fragment as the caging group, were designed to demonstrate single action PCT behavior, similar to the pyridine model complex [Ru(tpy)(Me<sub>2</sub>bpy)(py)](PF<sub>6</sub>)<sub>2</sub>,<sup>60</sup> as well as caged inhibitors of cysteine proteases<sup>64-65</sup> and CYP17A1<sup>23</sup> reported by us in prior studies. Analogs **9 – 11**, containing the [Ru(tpy)(L)] fragments as the photocaging groups, where L = dimethylbenzo[i]dipyrido[3,2-a:2',3'-c]phenazine (Me<sub>2</sub>dppn) and 3,6-dimethyl-10,15-diphenylbenzo[i]dipyrido[3,2-a:2',3'-c]phenazine (Me<sub>2</sub>Ph<sub>2</sub>dppn), were synthesized to provide dual action PCT/PDT capabilities. The reaction of **4** or **6** with [Ru(tpy)(Me<sub>2</sub>bpy)(Cl)]Cl<sup>66</sup> in a 1:1 mixture of EtOH and H<sub>2</sub>O at 80 °C gave

the photocaged inhibitors **7** and **8** in 75% and 63% yield, respectively, after chromatography over alumina. Complexes **9 – 11** were obtained by treating **4** or **6** with  $[\text{Ru}(\text{tpy})(\text{Me}_2\text{dppn})\text{Cl}]\text{Cl}^{67}$  or  $[\text{Ru}(\text{tpy})(\text{Ph}_2\text{Me}_2\text{dppn})\text{Cl}]\text{Cl}^{68}$  in a 1:1 mixture of EtOH and H<sub>2</sub>O at 80 °C in 48–61% yield after chromatography over alumina. The ligands Me<sub>2</sub>dppn and Me<sub>2</sub>Ph<sub>2</sub>dppn found in complexes **9–11** were included to promote ligand dissociation (PCT) from the triplet ligand field (<sup>3</sup>LF) state(s) and singlet oxygen (<sup>1</sup>O<sub>2</sub>) generation for PDT from the dppn-centered <sup>3</sup>ππ\* excited state(s). Importantly, we were motivated to use these ligands because our prior studies confirmed that dual action PCT/PDT behavior was necessary to achieve efficient death of triple negative breast cancer cells in 3D pathomimetic assays.<sup>65</sup>

**Scheme 1.** Synthesis (A) and structures (B) of Ru(II)-caged CYP3A4 inhibitors **7–11**



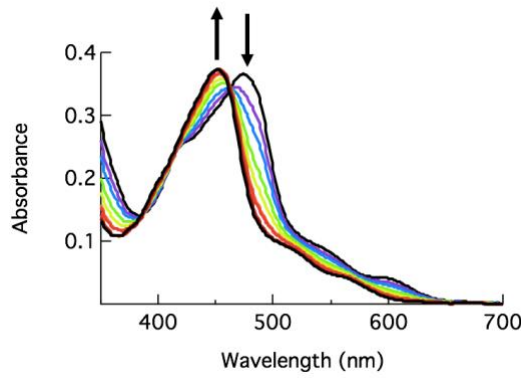
Complexes **7** – **11** were characterized by multiple methods, including electronic absorption, <sup>1</sup>H NMR, COSY and IR spectroscopies and electrospray ionization mass spectrometry (ESI-MS). The electronic absorption spectra of **7** and **8** exhibit maxima at 474 nm ( $\varepsilon = 7700 \text{ M}^{-1}\text{cm}^{-1}$ ) and 470 nm ( $\varepsilon = 9700 \text{ M}^{-1}\text{cm}^{-1}$ ), respectively, that are in good agreement with the corresponding pyridine model complex [Ru(tpy)(Me<sub>2</sub>bpy)(py)](PF<sub>6</sub>)<sub>2</sub>.<sup>60</sup> Likewise, the electronic absorption spectra of **9** ( $\lambda_{\text{max}}$  485 nm,  $\varepsilon = 13,500 \text{ M}^{-1}\text{cm}^{-1}$ ) and **10** ( $\lambda_{\text{max}}$  480 nm,  $\varepsilon = 12,000 \text{ M}^{-1}\text{cm}^{-1}$ ) show maxima consistent with [Ru(tpy)(Me<sub>2</sub>dppn)(py)](PF<sub>6</sub>)<sub>2</sub>.<sup>69</sup> The electronic absorption spectrum of **11** exhibits a maximum at 491 nm ( $\varepsilon = 13,500 \text{ M}^{-1}\text{cm}^{-1}$ ) that is slightly red-shifted compared to those of **9** and **10**, which agrees well with data for [Ru(tpy)(Ph<sub>2</sub>Me<sub>2</sub>dppn)(py)](PF<sub>6</sub>)<sub>2</sub>.<sup>68</sup> NMR spectra of complexes **7** – **11** show resonances ranging from 10–1 ppm that are consistent with the presence of the Ru(II)-caging groups, as well as peaks that are attributed to inhibitors **4** and **6** present in these structures. In particular, spectra for complexes **7**–**11** show singlets in the region of 2.5–1.0 ppm that are consistent with the two diasterotopic methyl groups present in the ligands Me<sub>2</sub>bpy, Me<sub>2</sub>dppn and Ph<sub>2</sub>Me<sub>2</sub>dppn. Methyl groups on the same face of the Ru(tpy) plane as the monodentate pyridyl ring are shifted upfield by ~0.7 ppm relative to resonances below that plane due to the shielding effect of the pyridyl ring; these shifts are similar to other photocaged complexes we have characterized in the past.<sup>23, 64–65</sup> Mass spectra of the photocaged complexes show major peaks with suitable isotope patterns with *m/z* values consistent with that expected for parent molecular dications [Ru(tpy)(Me<sub>2</sub>bpy)(**4**)]<sup>2+</sup> (**7**, *m/z* = 474) and [Ru(tpy)(Me<sub>2</sub>bpy)(**6**)]<sup>2+</sup>(**8**, *m/z* = 526) and the monocations ([Ru(tpy)(Me<sub>2</sub>dppn)(**4**)]Cl)<sup>+</sup> (**9**, *m/z* = 1159), ([Ru(tpy)(Me<sub>2</sub>dppn)(**6**)]Cl)<sup>+</sup> (**10**, *m/z* = 1263) and ([Ru(tpy)(Ph<sub>2</sub>Me<sub>2</sub>dppn)(**6**)]Cl)<sup>+</sup> (**11**, *m/z* = 1415). Taken together these data are consistent with the structural assignments shown in Scheme 1.

## Photochemistry

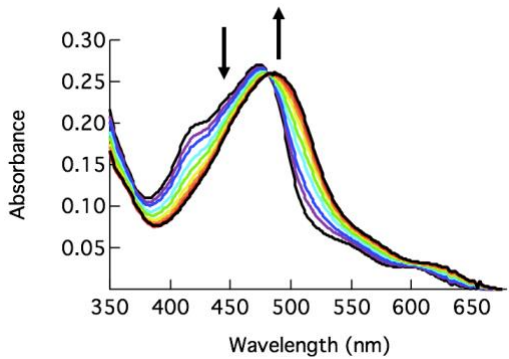
The irradiation of **7** effectively liberates **4**, resulting in ligand exchange with a solvent molecule, generating the corresponding  $[\text{Ru}(\text{tpy})(\text{Me}_2\text{bpy})(\text{L})]^{2+}$  ( $\text{L} = \text{H}_2\text{O}$  or  $\text{CH}_3\text{CN}$ ) product in  $\text{H}_2\text{O}$  or  $\text{CH}_3\text{CN}$ , respectively **under  $\text{N}_2$  atmosphere**. Photoactivated ligand exchange ( $\lambda_{\text{irr}} = 500 \text{ nm}$ ) of **7**, with absorption maximum at 474 nm, results in a blue shift to 450 nm in  $\text{CH}_3\text{CN}$  (Figure 2A) and a red shift to 495 nm in  $\text{H}_2\text{O}$  (Figure 2B). The resulting absorption maxima are consistent with the formation of the corresponding product with a coordinated  $\text{CH}_3\text{CN}$  or  $\text{H}_2\text{O}$  molecule.<sup>23,60,70</sup> Similarly, the irradiation of **8** with 500 nm light in  $\text{CH}_3\text{CN}$  resulted in a decrease in 470 nm absorption and a concomitant increase at 455 nm. This hypsochromic shift in the metal-to-ligand charge transfer (MLCT) band is consistent with the substitution of **6** coordinated to the Ru(II) metal through a pyridine unit for a  $\text{CH}_3\text{CN}$  solvent molecule (Figure S8).<sup>23,70</sup> The presence of an isosbestic point at 463 nm indicates the formation of a single photoproduct,  $[\text{Ru}(\text{tpy})(\text{Me}_2\text{bpy})(\text{CH}_3\text{CN})]^{2+}$ . Comparable changes in the electronic absorption spectra of **9 – 11** are observed under similar experimental conditions (Figures S9–11).

**Figure 2.** Changes to the electronic absorption spectra of **7** as a function of irradiation time ( $\lambda_{\text{irr}} = 500 \text{ nm}$ ) in  $\text{CH}_3\text{CN}$  for 0–12 min (A) and in  $\text{H}_2\text{O}$  for 0–20 min (B) **under  $\text{N}_2$  atmosphere**.

A



B



The quantum yields ( $\Phi_{LE}$ ) for the ligand-exchange with a solvent molecule for **7 – 11** are listed in Table 1. For **7**,  $\Phi_{LE}$  values of 0.15(1) in  $\text{H}_2\text{O}$  and 0.31(1) in  $\text{CH}_3\text{CN}$  were measured upon 500 nm irradiation (Table 1). The value in  $\text{H}_2\text{O}$  is lower than that observed for  $[\text{Ru}(\text{tpy})(\text{Me}_2\text{bpy})(\text{py})]^{2+}$ ,  $\Phi_{LE} = 0.41(2)$ , but similar in  $\text{CH}_3\text{CN}$ ,  $\Phi_{LE} = 0.33(1)$ .<sup>60</sup> The lower quantum yield observed for **7** vs  $[\text{Ru}(\text{tpy})(\text{Me}_2\text{bpy})(\text{py})]^{2+}$  in  $\text{H}_2\text{O}$  can be attributed to the lower solubility of CYP3A4 inhibitor **4** in water as compared to pyridine, which reduces the ability of the former to escape the solvent cage upon release from Ru(II). Similarly, Table 1 reveals a  $\Phi_{LE}$  value **lower for 8 relative to 7 in  $\text{CH}_3\text{CN}$** , which likely arises from the larger size and poorer solubility of inhibitor **6** as compared to **4**. Following the same trend as **7** and **8**, complex **9** containing the CYP3A4 inhibitor **4** showed ~2-fold more efficient photorelease than its analog **10** containing the bulky inhibitor **6**. Complex **11** showed the most efficient photorelease in the **9 – 11** subseries, which is consistent with our earlier observations showing that complexes containing arylated  $\text{Me}_2\text{dppn}$  derivatives, such as  $\text{Ph}_2\text{Me}_2\text{dppn}$ , undergo more efficient photorelease than  $\text{Me}_2\text{dppn}$  derivatives.<sup>68</sup> Complex **7** exhibits the highest ligand exchange quantum yield of the five complexes. It is hypothesized that the initially populated  $^1\text{MLCT}$  excited state intersystem crosses to the triplet manifold, populating both the lowest-energy dppn  $^3\pi\pi^*$  state and the  $^3\text{LF}$  states in **9 – 11**, and the population of the latter results in ligand dissociation. The absence of a lowest-energy

long-lived dppn-centered  $^3\pi\pi^*$  excited state in **7** and **8** precludes the bifurcation of intersystem crossing, resulting in an increased population of the  $^3\text{LF}$  state and, consequently, greater photoinduced ligand exchange quantum yield as compared to **9 – 11**.<sup>69, 71</sup>

**Table 1.** Quantum yields of ligand exchange ( $\Phi_{\text{LE}}$ ) and singlet oxygen ( $\Phi_{\Delta}$ ) production for **7-11**.

Complex	$\Phi_{\text{LE}}^a$	$\Phi_{\Delta}^b$
<b>7</b>	0.15(1) <sup>c</sup>	–
<b>7</b>	0.31(1)	–
<b>8</b>	0.13(2)	–
<b>9</b>	0.024(4)	0.59(6)
<b>10</b>	0.014(3)	0.57(6)
<b>11</b>	0.061(8)	0.80(7)
$[\text{Ru}(\text{tpy})(\text{Me}_2\text{dppn})(\text{L})]^{2+}^d$	0.073(1)	0.57(7)

<sup>a</sup> In  $\text{CH}_3\text{CN}$ ,  $\lambda_{\text{irr}} = 500$  nm,  $\text{N}_2$  atmosphere. <sup>b</sup> In  $\text{MeOH}$ ,  $\lambda_{\text{irr}} = 460$  nm, determined with diphenylisobenzofuran (DPBF)  $^1\text{O}_2$  probe under  $\text{N}_2$ .

<sup>c</sup> In  $\text{H}_2\text{O}$ ,  $\lambda_{\text{irr}} = 500$  nm. <sup>d</sup> From ref. 72;  $\text{L}$  = imatinib.

In addition to photosubstitution of the monodentate ligand, **9 – 11** produce cytotoxic  $^1\text{O}_2$  through the population of the lowest-energy, long-lived  $^3\pi\pi^*$  excited state upon irradiation. The quantum yields for  $^1\text{O}_2$  production,  $\Phi_{\Delta}$ , by **9 – 11** of 0.59(6), 0.57(6), and 0.80(7), respectively, are comparable to those of other dual-activity complexes possessing dppn ligands, such as  $[\text{Ru}(\text{tpy})(\text{Ph}_2\text{Me}_2\text{dppn})(\text{py})](\text{PF}_6)_2$ <sup>68</sup> and  $[\text{Ru}(\text{tpy})(\text{Me}_2\text{dppn})(\text{imatinib})]^{2+}$  (Table 1).<sup>70, 72</sup> Our prior studies established that the Ru(II) photocaging group  $[\text{Ru}(\text{tpy})(\text{Me}_2\text{bpy})]$  found in **7** and **8** does not generate  $^1\text{O}_2$  either before or after photorelease because its excited state lifetime is too short to undergo bimolecular reactions, as is the case with other Ru(II) complexes containing the tpy ligand or those that undergo facile ligand photodissociation.<sup>69, 70</sup>

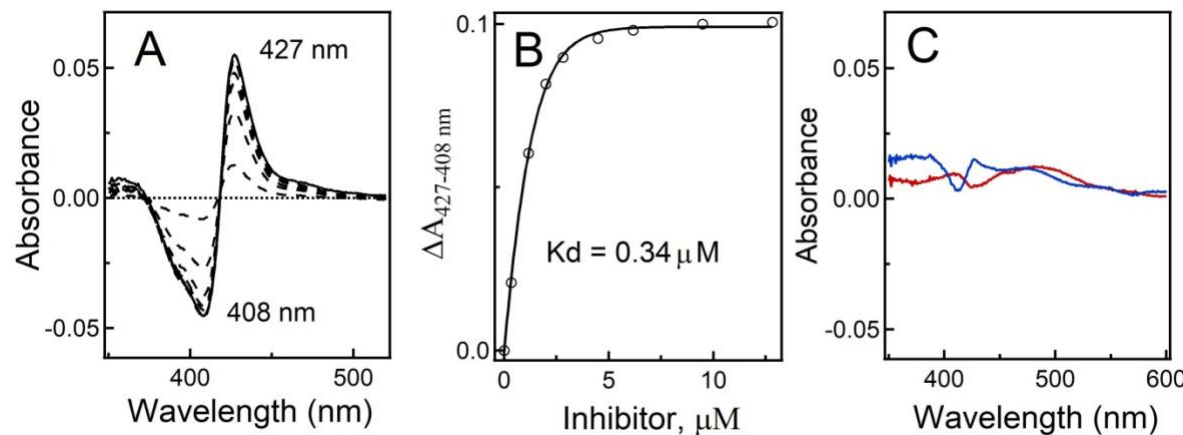
The stability of **7 – 11** was assessed in cell growth media at 37 °C as previously described.<sup>73-74</sup> No spectral changes were observed for **7 – 9** in the dark (Figures S18 – S24) over a course of 24 h, consistent with the exceptional stability of Ru(II)-caged aromatic heterocycles. Complexes **10** and **11** did show some spectral changes over the 24 h period that are consistent with compound precipitation from solution and/or thermal ligand dissociation.

### CYP3A4 Inhibition Studies

After establishing that CYP3A4 inhibitor **4** is photochemically released from its Ru(II) cage **7**, the complex was evaluated against the purified CYP3A4 enzyme under dark conditions and upon irradiation. Stock solutions of **7** were left in the dark or exposed to light ( $\lambda_{\text{irr}} = 400\text{--}700$  nm,  $t_{\text{irr}} = 40$  min) before titrating against soluble CYP3A4 (residues 3-22 deleted). Heme binding to the iron center in CYP3A4 was monitored via electronic absorption spectroscopy. Data indicated that the caged inhibitor **7** effectively released **4** from the ruthenium center upon irradiation with visible light, allowing the pyridine functional group of **4** to bind to CYP3A4 via a type II heme ligation. The difference spectra were similar to those obtained for the free **4** inhibitor and showed an increase in intensity at 427 nm and a decrease at 407 nm, consistent with type II binding (Figure 3A), where substitution of the water ligand with pyridine drives conversion of the heme center from a high spin to low spin ferric state. Hyperbolic fitting to the titration plot resulted in  $K_d = 340$  nM for **7** under irradiation (Figure 3B). In contrast, no spectral evidence for type II binding was observed during titration of CYP3A4 with **7** under dark conditions. Minor perturbations to the absorption spectra were attributed to the Ru(II) complex, strongly absorbing at 400–500 nm, rather than type II binding (Figure 3C). Similarly, the titration of CYP3A4 with a control compound, [Ru(tpy)(Me<sub>2</sub>bpy)(Cl)]Cl, led to minor spectral changes. Taken together, these

data indicate that type II heme binding is effectively blocked by Ru(II) caging, and that irradiation with visible light triggers the release of inhibitor **4**, enabling its ligation to the CYP3A4 heme.

**Figure 3.** Equilibrium titration of CYP3A4 with **7** under light and dark conditions<sup>a</sup>

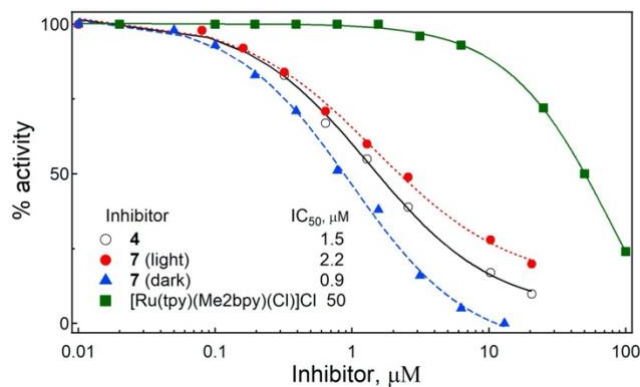


<sup>a</sup>(A) Difference spectra recorded during titration of recombinant CYP3A4 with **7** under light conditions; (B) titration plot; dissociation constant ( $K_d$ ) was calculated by fitting the data to a hyperbolic equation:  $\Delta A = \Delta A_{\max} \times [\text{ligand}] / (K_d + [\text{ligand}])$ , where  $\Delta A_{\max}$  is the maximal absorbance change, and  $\Delta A$  and  $[\text{ligand}]$  are the absorbance change and ligand concentration after each titrant addition, respectively; (C) difference spectra recorded in control experiments, where CYP3A4 was mixed with 10  $\mu\text{M}$  **7** (blue) or 10  $\mu\text{M}$   $[\text{Ru}(\text{tpy})(\text{Me}_2\text{bpy})\text{Cl}]^+$  (red) in the dark, show the lack of spectral changes characteristic for type II N-Fe ligation.

Next, compound **7** was evaluated for its ability to inhibit CYP3A4 activity under light and dark conditions. The free inhibitor **4** and  $[\text{Ru}(\text{tpy})(\text{Me}_2\text{bpy})\text{Cl}]^+$  were included as controls.  $IC_{50}$  values were determined using a fluorogenic assay that monitors the *O*-debenzylation of 7-benzyloxy-4-trifluoromethylcoumarin (BFC), with 100% activity set at vehicle (DMSO) only. After treatment with visible light ( $\lambda_{\text{irr}} = 400\text{--}700 \text{ nm}$ ,  $t_{\text{irr}} = 40 \text{ min}$ ), **7** inhibited CYP3A4 nearly as well as free inhibitor **4** ( $IC_{50}$  of 2.2  $\mu\text{M}$  and 1.5  $\mu\text{M}$ , respectively), which agrees well with the spectral data (Figures 2 and 3) showing that **4** is released from **7** upon irradiation. However, to our surprise, the intact **7** was more potent in the dark ( $IC_{50}$  of 0.9  $\mu\text{M}$ ; Figure 4), suggesting that the

Ru(II) complex could bind to CYP3A4 more strongly than free **4**. Control experiments with  $[\text{Ru}(\text{tpy})(\text{Me}_2\text{bpy})(\text{Cl})]\text{Cl}$  ( $\text{IC}_{50} > 50 \mu\text{M}$ ) showed that CYP3A4 inhibition was not due to just the Ru(II) fragment. Taken together, these data indicate that **7** is a stronger inhibitor when kept in the dark as compared to under irradiation.

**Figure 4.** Inhibition of the BFC activity of recombinant CYP3A4 by **4**, **7** and the control complex  $[\text{Ru}(\text{tpy})(\text{Me}_2\text{bpy})(\text{Cl})]\text{Cl}^a$

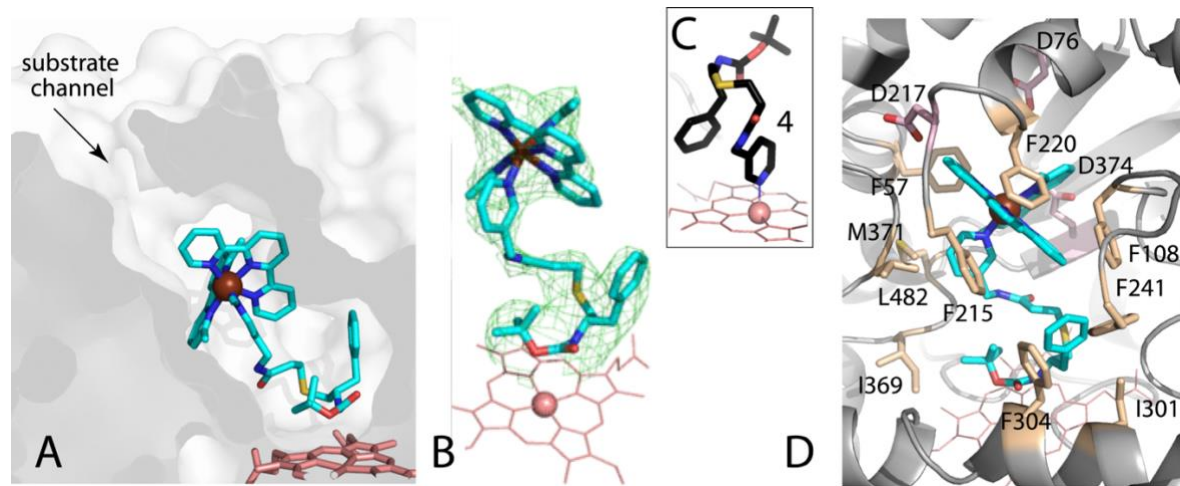


<sup>a</sup>Inhibitory assays were conducted at room temperature in a reconstituted system containing 0.2  $\mu\text{M}$  CYP3A4 and 0.3  $\mu\text{M}$  cytochrome P450 reductase by monitoring formation of a fluorescent product. The remaining activity was calculated relative to the DMSO-containing sample, used as a control (100% activity). The IC<sub>50</sub> values were derived from fittings to the [% activity] vs. [inhibitor] plots.

To confirm that the intact **7** is able to access the active site, we crystallized the CYP3A4-**7** complex and solved the structure to 2.5  $\text{\AA}$  resolution. Indeed, **7** was bound in a well-defined manner within the active site (Figure 5). The inhibitor tail curls above the heme without direct binding to the iron center, while the bulky Ru(II) cage stacks inside the substrate channel. Protein-ligand interactions are predominantly hydrophobic. The inhibitor tail is surrounded by Phe241, Ile301, Phe304 and Ile369, whereas the ligands of the  $[\text{Ru}(\text{tpy})(\text{Me}_2\text{bpy})]$  cage fragment stack with Phe108, Phe215 and Phe220 and is in close contacts with Phe57, Leu217, Met371 and Leu482. The anionic residues Asp76, Asp217 and Glu374 may also help to strengthen the inhibitory

complex by creating favorable electrostatic interactions with the dicationic Ru(II) fragment. Importantly, the **7** N-pyridine does not bind to the heme iron because it is stably coordinated to Ru(II). This structure is highly valuable because it demonstrates that strong CYP3A4 inhibition by the intact, non-irradiated chimeric compound does not require Fe-N ligation.

**Figure 5.** Crystal structure of CYP3A4 bound to **7** at 2.5 Å resolution.<sup>a</sup>



<sup>a</sup>(A) Slice through the CYP3A4 molecule showing orientation of **7**, (B) omit electron density map for **7** at 3σ level, (C) the binding mode of free compound **4** (4D78 structure) shown for comparison, and (D) residues interacting with **7**: hydrophobic in beige and acidic in pink.

Based on the finding that **7** potently inhibits CYP3A4 in the dark, the inhibitory assays for complexes **8 – 11** were conducted under both dark and light conditions ( $\lambda_{\text{irr}} = 400\text{--}700\text{ nm}$ ,  $t_{\text{irr}} = 40\text{ min}$ ). IC<sub>50</sub> values for the BFC activity of CYP3A4 are presented in Table 2. Complex **8**, which contains inhibitor **6**, inhibits CYP3A4 nearly to the same extent under dark and light conditions, giving a phototherapy index (PI) of 1.1. Interestingly, under dark conditions, **8** inhibits CYP3A4 roughly twice as potently as **7** (IC<sub>50</sub> of ~400 nM). Since **8** willingly co-crystallized with CYP3A4, we also determined the CYP3A4-**8** complex structure. Despite the fact that resolution was similar, 2.5 Å, **8** was poorly defined and the electron density around the ligand was discontinuous, which can be attributed to multiple binding modes. Nonetheless, the Ru-center and the core of the

inhibitor tail could be located, allowing ligand fitting. As shown in Figure S12, the [Ru(tpy)(Me<sub>2</sub>bpy)] cage binds within the same pocket in the substrate channel. The inhibitor end-portion, in turn, similarly curls above the heme. Again, the complex is largely stabilized by aromatic stacking and hydrophobic interactions mediated by Phe57, Phe108, Phe220, Phe221, Phe241 and Phe304.

Similar to **7**, the Me<sub>2</sub>dppn complexes **9** and **10** inhibited CYP3A4 more potently under dark than light conditions, but at lower concentrations than **7**. Dark IC<sub>50</sub> values for **9** and **10** were in the 250-280 nM range, with PI values of 0.30 and 0.61, respectively. Attempts to co-crystallize **9** and **10** with CYP3A4 were unsuccessful. Examination of inhibitors' solutions showed that both **9** and **10** have tendency to aggregate. Compound aggregation in solution can lead to false positives for enzyme inhibition, e.g. by trapping active enzyme within colloidal particles that block access of substrates.<sup>75</sup> One way to distinguish between specific and nonspecific inhibition is to add detergents or other solubilizing agents to enzymatic assays. Therefore, we screened several detergents known to break up aggregates, including CHAPS, CYMAL-5, octylglucoside and cyclodextrin. CYP3A4 was highly sensitive to detergents, with most detergents abolishing the BFC activity even in the absence of inhibitors. However, CYP3A4 preserved ~80% activity in the presence of 2% cyclodextrin. The latter agent was used for re-evaluation of **10** and, as we found, reversed the trend: dark IC<sub>50</sub> = 1.02 μM, light IC<sub>50</sub> = 0.44 μM, giving a PI of 2.3. Thus, aggregation was at least partially responsible for CYP3A4 inhibition by **10** in the dark. Importantly, the higher PI with 2% cyclodextrin was due to a higher IC<sub>50</sub> for **10** in the dark; light data with and without 2% cyclodextrin were virtually the same and agreed well with those for free **6**. Finally, the bulky Ph<sub>2</sub>Me<sub>2</sub>dppn-containing complex **11** showed an improved PI value, 1.90, as compared to PI = 0.61

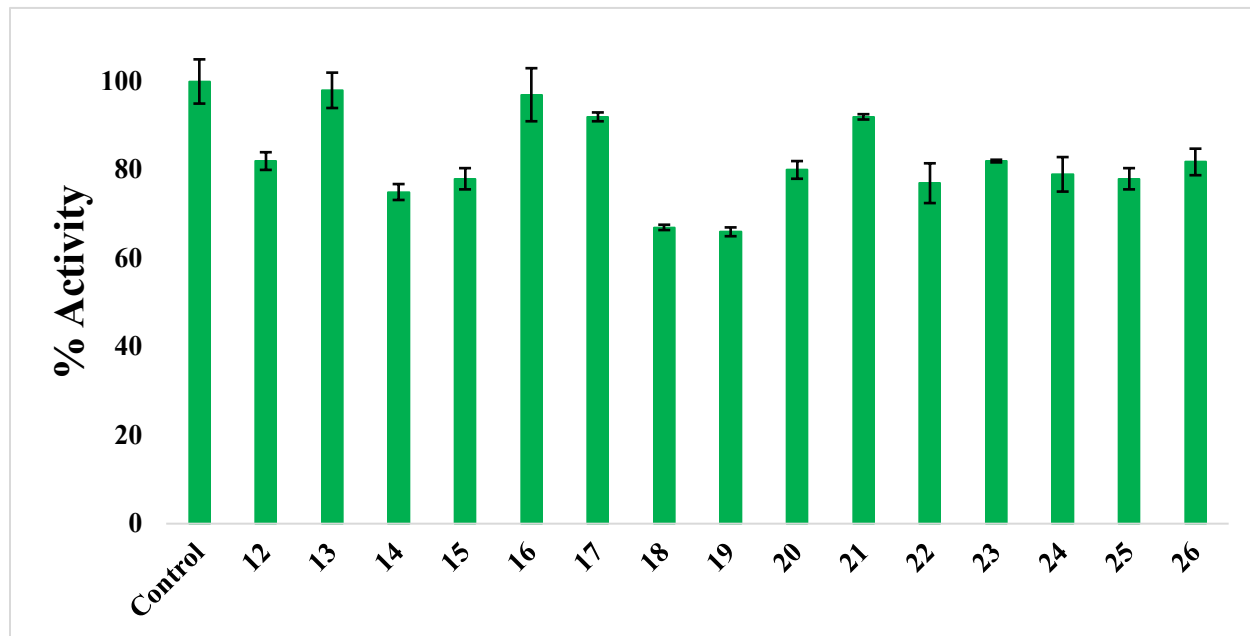
for **10**, implying that the larger caging group [Ru(tpy)(Ph<sub>2</sub>Me<sub>2</sub>dppn)] disfavors binding to the CYP3A4 active site.

**Table 2.** IC<sub>50</sub> values (μM) for CYP3A4 inhibition by **4**, **6** and **7-11** under dark and light conditions.<sup>a</sup>

Compound	Dark IC <sub>50</sub>	Light IC <sub>50</sub> <sup>b</sup>	PI
<b>4</b>	1.54	nd	—
<b>6</b>	0.40	nd	—
<b>7</b>	0.9	2.2	0.41
<b>8</b>	0.40	0.36	1.1
<b>9</b>	0.25	0.84	0.30
<b>10</b>	0.28	0.46	0.61
<b>10<sup>c</sup></b>	1.02	0.44	2.3
<b>11</b>	0.40	0.21	1.90

<sup>a</sup>Inhibitory assays for the BFC activity were conducted at room temperature in a reconstituted system containing 0.2 μM CYP3A4 and 0.3 μM cytochrome P450 reductase by monitoring formation of a fluorescent product. Stock solutions of **4**, **6**, **7-11** were prepared in DMSO. The activity remaining was calculated relative to the DMSO-containing sample, used as a control (100% activity). The IC<sub>50</sub> values were derived from fittings to the [% activity] vs. [inhibitor] plots. The standard error was <10%. <sup>b</sup>Light conditions ( $\lambda_{\text{irr}} = 400\text{--}700\text{ nm}$ ,  $t_{\text{irr}} = 40\text{ min}$ ). <sup>c</sup>Assay containing 2% cyclodextrin.

**Figure 6.** CYP 3A4 Inhibition with a panel of Ru(II) complexes at 1  $\mu$ M against purified enzyme<sup>a</sup>



<sup>a</sup>Inhibition of recombinant CYP3A4 with various complexes; Compounds are [Ru(bpy)<sub>3</sub>]Cl<sub>2</sub> (**12**), [Ru(phen)<sub>3</sub>](PF<sub>6</sub>)<sub>2</sub> (**13**), [Ru(bpy)<sub>2</sub>(phpy)]Cl (**14**), [Ru(bpy)<sub>2</sub>(acac)]PF<sub>6</sub> (**15**), [Ru(bpy)<sub>2</sub>(bete)](PF<sub>6</sub>)<sub>2</sub> (**16**), [Ru(bpy)<sub>2</sub>(bpte)]Cl<sub>2</sub> (**17**), [Ru(bpy)<sub>2</sub>(dppn)](PF<sub>6</sub>)<sub>2</sub> (**18**), [Ru(dppz)<sub>2</sub>(bpy)]Cl<sub>2</sub> (**19**), [Ru( $\eta^6$ -p-cym)(DBM)Cl] (**20**), [Ru( $\eta^6$ -p-cym)(hfa)Cl] (**21**), [Ru( $\eta^6$ -p-cym)(bpy)Cl]Cl (**22**), [Ru(bpy)<sub>2</sub>(NHC-OMe)]PF<sub>6</sub> (**23**), [Ru(bpy)<sub>2</sub>(NHC-COOEt)]PF<sub>6</sub> (**24**), [Ru(tpy)(dppn)(py)](PF<sub>6</sub>)<sub>2</sub> (**25**), [Ru(tpy)(acac)(py)]PF<sub>6</sub> (**26**). See Figure S25 for structures.

In order to characterize the scope of CYP3A4 inhibition, we screened a library of 15 compounds, consisting of a diverse set of mono- and dicationic Ru(II) complexes (**12 – 26**, Figure 6, see Figure S25 for structures), against the purified enzyme. All complexes were screened against CYP3A4 under dark conditions at a concentration of 1  $\mu$ M. Activities were determined using BFC as a substrate and expressed as percentage vs. vehicle (DMSO) control. Thirteen complexes failed to decrease CYP3A4 activity below 75% at 1  $\mu$ M concentration, confirming that potent CYP3A4 inhibition is not a general property of Ru(II) complexes. Only two compounds, [Ru(bpy)<sub>2</sub>(dppn)](PF<sub>6</sub>)<sub>2</sub> (**18**) and [Ru(dppz)<sub>2</sub>(bpy)]Cl<sub>2</sub> (**19**) reduced CYP3A4 activity below 75%

at 1  $\mu$ M concentration. Collectively, these data reveal complex structure-activity relationships for inhibition of CYP3A4 by Ru(II) complexes that warrant further investigation.

To gain further insight into the potential biological applications of Ru(II)-based CYP inhibitors, we determined IC<sub>50</sub> values for **4** and complexes **7** and **9** against microsomal CYP3A4 and two other major drug metabolizing enzymes, CYP1A2 and CYP2C9,<sup>76</sup> using commercially available inhibitor screening kits (BioVision, Table 3). It should be pointed out that protein concentration and CYP:reductase ratios in the BioVision kits and our soluble reconstituted system were different, owing to which data in Tables 2 and 3 cannot be directly compared. For microsomal CYP3A4, inhibitor **4** was active in the nM range, with the IC<sub>50</sub> values being nearly the same (~200 nM) under dark and light conditions. Complex **7** also inhibited CYP3A4 at nanomolar concentrations but more potently under dark vs. light conditions, following the same trend as data presented for **7** presented in Table 2. Importantly, both **4** and **7** were much weaker inhibitors of CYP1A2 and CYP2C9. The selectivity of **4** for CYP3A4 was ~500-fold higher, whereas **7** inhibited CYP3A4 ~70-to-130-fold and 60-to-76-fold stronger than the other CYPs under dark and light conditions (460–470 nm; 20 min), respectively. A multi-fold difference in IC<sub>50</sub> measured for **4** and **7** under dark conditions suggests some influence of the released Ru(II) cage in the inhibition. The respective data were also collected for Ru(II) complex **9**, which contains the same inhibitor **4** linked to the bulky and more hydrophobic photocaging group [Ru(tpy)(Me<sub>2</sub>dppn)]. Compared to **7**, the inhibitory potency of **9** for microsomal CYP3A4 was ~8- and 5-fold lower under dark and light conditions, respectively, and its selectivity for other isoforms could not be accurately measured due to solubility problems. Even so, there was a common trend, as all three compounds displayed higher specificity for CYP3A4 albeit to a different extent.

**Table 3.** IC<sub>50</sub> values (μM) for **4**, **7** and **9** against microsomal CYP3A4, CYP1A2 and CYP2C9 under dark and light conditions.<sup>a</sup>

Compound	CYP3A4		CYP1A2		CYP2C9		Selectivity	
	Dark	Light	Dark	Light	Dark	Light	1A2/3 A4	2C9/3A 4
							Dark (Light)	Dark (Light)
<b>4</b>	0.183 ± .01	0.232 ± .018	>100	ND	87 ± 2	ND	566 (ND)	475 (ND)
<b>7</b>	0.217 ± .011	0.301 ± .001	28 ± 2	23 ± 1	15 ± 3	18 ± 1	129 (76)	69 (60)
<b>9</b>	1.7 ± 0.1	1.6 ± 0.1	>10	>10	>10	>10	>5.9 (>6.3)	>5.9 (>6.3)

<sup>a</sup>IC<sub>50</sub> values determined using CYP3A4, CYP1A2 or CYP2C9 Inhibitor Screening Kits (BioVision) following manufacturer protocols. Stock solutions of **4**, **7** or **9** were prepared in MeCN, plated and combined with assay buffer and irradiated with a blue LED light source (*t*<sub>irr</sub> = 20 min,  $\lambda$ <sub>irr</sub> = 460–470 nm, **56 J/cm<sup>2</sup>**) or left in the dark. Experiments with compound **9** did not exceed 10 μM due to solubility limitations in assay buffer. Percent activities were determined vs. vehicle control. IC<sub>50</sub> values were determined using Igor Pro graphing software. Data are average of three experiments, errors are standard deviations.

## Biological Studies

Studies on the interaction of **7 – 11** with isolated CYP3A4 showed that inhibition can be achieved via blockage of the active site by the intact caged compounds, light-activated release of the inhibitory fragment and its subsequent heme ligation, and efficient <sup>1</sup>O<sub>2</sub> generation. However, questions remained regarding the role of aggregation *vs* direct inhibition of CYP3A4 in the dark, due to sensitivity of the recombinant enzyme to common detergents. These challenges prompted us to utilize an *in vitro* cell-based assay to probe for CYP3A4 inhibition by our compounds. Importantly, prior studies demonstrated that CYP3A4 inhibitors work synergistically with

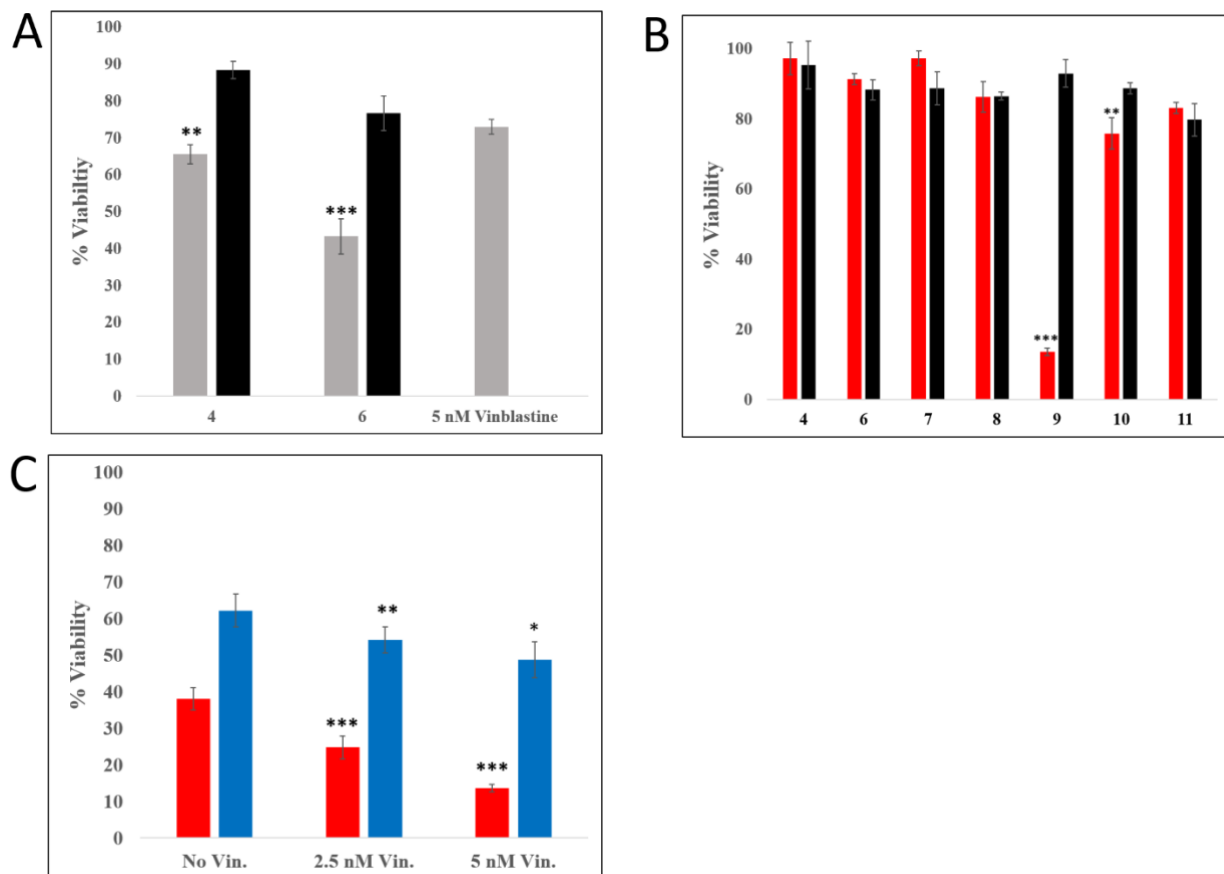
microtubule-destabilizing drugs in cancer cells.<sup>77-78</sup> We chose to evaluate our compounds in DU-145 prostate cancer cells because (i) they have high levels of CYP3A4 expression; (ii) prior studies showed synergism between the CYP3A4 inhibitor ketoconazole and vinblastine,<sup>77</sup> a drug commonly used in combination therapies for various cancers, and (iii) utilization of a validated protocol for *in vitro* detection of synergism between a chemotherapeutic drug and CYP3A4 inhibitors would provide a reliable cell-based assay for evaluation of our compounds. Vinblastine binds to tubulin and stops production of microtubules, leading to M-phase specific cell cycle arrest. Synergism between vinblastine and ketoconazole was previously achieved by blocking CYP3A4-dependent vinblastine metabolism in several prostate cancer cell lines.<sup>77</sup> Based on this knowledge, we designed experiments with DU-145 cells and our panel of compounds. First, free CYP3A4 inhibitors **4** and **6** (5  $\mu$ M) were evaluated against DU-145 cells in the presence or absence of vinblastine (5 nM). Cells were treated with **4** or **6** and vinblastine or vehicle, and viability was assessed after 72 h by the 3-(4,5-dimethylthiazol-2-yl)-2,5-diphenyl tetrazolium bromide (MTT) assay. It was found that both **4** and **6** reduce viability of the DU-145 cells by up to ~40% in the presence of 5 nM vinblastine. This reduction of viability is similar to that observed with ketoconazole<sup>77</sup> and suggests the synergy between CYP3A4 inhibition and the microtubule-destabilizing drug (Figure 7A).

Next, inhibitors **4** and **6** were evaluated alongside the photocaged inhibitors **7 – 11** in the dark or with irradiation in the presence of vinblastine (5 nM). In these experiments, cells were treated with **4**, **6** or **7 – 11** (5  $\mu$ M) and kept in the dark for 1 h, then the media was replaced with media containing 5 nM vinblastine, and cells were irradiated with blue light (460–470 nm, 20 min) or left in the dark for 20 min. Viabilities were determined 72 h after light treatment by the MTT assay. As expected, results with the free inhibitors **4** and **6** were virtually identical under dark and

light conditions, **ruling out synergy between 4 or 6 and light**. In these experiments, synergy with **4** and **6** was less pronounced compared to incubations where **4** or **6** were left with cells for the full 72 h without media replacement (Figure S13), which may indicate slower uptake of these inhibitors by DU-145 cells. Among the investigated compounds, complex **9**, which not only releases the CYP3A4 inhibitor **4** (PCT) but also generates  $^1\text{O}_2$  (PDT), showed the strongest response by reducing viability to  $\sim 10\%$  in the light compared to  $\sim 90\%$  in the dark (Figure 7B). Again, results were less pronounced when **7 – 11** were left with DU-145 cells for the full 72 h without media replacement (Figure S13), further indicating that cell uptake is slower for some of the Ru(II) complexes. Nonetheless, complex **9** showed a strong response with media replacement after only 1 h, which supports the ability of **9** to penetrate DU-145 cells within that timeframe.

Next, we probed the impact of CYP3A4 inhibition in cell-induced toxicity with vinblastine. Complex **9** was compared side-by-side with the  $[\text{Ru}(\text{tpy})(\text{Me}_2\text{dppn})(\text{py})](\text{PF}_6)_2$  complex (**27**), which generates  $^1\text{O}_2$  just as efficiently<sup>69</sup> but serves as a control by releasing pyridine rather than the CYP3A4 inhibitor **4**. Experiments with **27** were important to carry out because prior studies demonstrated that PDT can work synergistically with microtubule-targeting drugs.<sup>79</sup> The results in Figure 7C show that **9** (5  $\mu\text{M}$ ) produces a strong, dose-dependent synergy with vinblastine (0–5 nM), whereas less toxic **27** (5  $\mu\text{M}$ ) does not. These data suggest that CYP3A4 inhibition is synergistic with PDT and vinblastine.

**Figure 7.** Cellular viability studies with compounds **4**, **6 – 11** and **27** in DU-145 prostate adenocarcinoma cells<sup>a</sup>



<sup>a</sup> DU-145 cells were seeded in a 96-well plate at a density of 7000 cells per well and incubated overnight (~18 h). **(A)** The media was aspirated from each well, and quadruplicate wells were treated with media containing either **4** or **6** (5  $\mu$ M) in 1% DMSO (Black) or co-treated with vinblastine (5 nM) (Gray). After 72 h of incubation at 37 °C, MTT assay was performed. Viability data were obtained by averaging blank-normalized absorbance values for control cells and expressing average absorbance for the treated samples as percent control. P-values are vs. 5 nM vinblastine alone. **(B)** The media was aspirated from each well and octuplicate wells were treated with media containing one of compounds **4** or **6–11** (5  $\mu$ M) in 1% DMSO. After 1 h of incubation at 37 °C, the media was aspirated and replaced with media containing vinblastine (5 nM). The plates were irradiated using a blue LED light source ( $t_{\text{irr}} = 20$  min,  $\lambda_{\text{irr}} = 460–470$  nm, **56 J/cm<sup>2</sup>**) (Red) or left in the dark (Black) and incubated for 72 h. MTT assay was then performed. Viability data were obtained by averaging blank-normalized absorbance values for control cells and expressing average absorbance for the treated samples as percent control. P-values are vs. dark viabilities for each compound. **(C)** The media was aspirated from each well and octuplicate wells were treated with media containing either compound **9** (Red) or **27** (Blue) (5  $\mu$ M) in 1% DMSO.

After 1 h of incubation at 37 °C, the media was aspirated and replaced with either vehicle or media containing vinblastine (2.5 nM or 5 nM) or vehicle. The plates were irradiated using a blue LED light source ( $t_{\text{irr}} = 20$  min,  $\lambda_{\text{irr}} = 460\text{--}470$  nm, 56 J/cm<sup>2</sup>) and then incubated for 72 h. MTT assay was then performed. Viability data were obtained by averaging blank-normalized absorbance values for control cells and expressing average absorbance for the treated samples as percent control. P-values are vs. 0 nM vinblastine (No Vin.) for each compound; \*\*\*P<0.01 \*\*P<0.05 \*P<0.10.

In order to quantify drug synergy, the Chou-Talalay method was applied, which is the field standard for assessing the synergy of a drug combination.<sup>80-83</sup> DU-145 cells were treated with either **4**, **7**, **9**, **27** or vinblastine alone over a range of concentrations to determine EC<sub>50</sub> (Table 4). Only for **9**, **27** and vinblastine the EC<sub>50</sub> values were < 25 μM under light conditions ( $t_{\text{irr}} = 20$  min,  $\lambda_{\text{irr}} = 460\text{--}470$  nm, 72 h MTT); in the dark, EC<sub>50</sub> for all compounds was > 25 μM. Next, DU-145 cells were treated with a combination of single concentrations of **9** or **27** and vinblastine over a range of concentrations spanning the EC<sub>50</sub> values under light conditions ( $t_{\text{irr}} = 20$  min,  $\lambda_{\text{irr}} = 460\text{--}470$  nm, 72 h MTT), resulting in a panel of 16 distinct combinations (Figure 8 for **9**, S14 for **27**). Viabilities for the single drug and combination treatments were compared against the vehicle control to measure the % effectiveness as the proportion between live and dead cells in a given treatment. Using the dose and effect for each mono-treatment and each combination, the combination index (CI) values for each treatment pair were calculated using Compusyn software (Figure 8).<sup>80</sup> CI values less than 1 indicate synergy, equal to 1 indicate an additive effect, and greater than 1 indicate antagonism. For compound **9**, 12 out of 16 combinations surveyed showed CI values <1, with the other four combinations showing CI values near 1, indicating high synergism between **9** and vinblastine under light conditions. In contrast, **27** showed weaker synergism under all concentrations surveyed under light conditions (Figure S14). Taken together, these data suggest that (i) **9** blocks intracellular metabolism of vinblastine via CYP3A4 inhibition,

and (ii) the CYP3A4 inhibition, PDT, and vinblastine act together and produce a stronger cytotoxic response in the DU-145 cells than the combination of PDT and vinblastine. Because microtubule-destabilizing drugs have deleterious side effects and narrow therapeutic indexes, the combination of localized CYP3A4 inhibition and PDT may prove to be a promising approach to achieve synergy and lower the doses of chemotherapeutic drugs like vinblastine.

**Table 4:** EC<sub>50</sub> values for **4**, **7**, **9**, and **27** in DU-145 cells<sup>a</sup>

Entry	Compound	EC <sub>50</sub> (μM)	
		Light	Dark
1	<b>4</b>	>25	>25
2	<b>6</b>	ND	17 ± 3
3	<b>7</b>	>25	>25
4	<b>9</b>	2.8 ± 1.0	>25
5	<b>27</b>	5.5 ± 0.8	>25
6	Vinblastine	8.3 ± 1.1 × 10 <sup>-3</sup>	ND

<sup>a</sup>EC<sub>50</sub> determination for compounds **4**, **6**, **7**, **9**, **27** and vinblastine were performed on DU-145 cells. Data are average of three independent experiments using quadruplicate wells; errors are standard deviations. After treatment, cells were incubated at 37 °C and 5% CO<sub>2</sub> for 1 h. Media was aspirated and replaced with vehicle. Cells were irradiated using a blue LED light source (*t*<sub>irr</sub> = 20 min,  $\lambda$ <sub>irr</sub> = 460–470 nm, 56 J/cm<sup>2</sup>) and incubated for 72 h. After that, viability was assessed by MTT assay. EC<sub>50</sub> values were obtained using Igor Pro graphing software for **4**, **6**, **7**, **9**, and **27** and with Compusyn software for vinblastine.

**Figure 8.** Chou-Talalay combination index heat map<sup>a</sup>

		Compound 9			
		10 $\mu$ M	5.0 $\mu$ M	2.5 $\mu$ M	1.0 $\mu$ M
Vinblastine	10 nM	0.52	0.51	0.86	0.72
	5.0 nM	0.66	0.48	1.07	1.08
	2.5 nM	0.65	0.58	0.91	0.84
	1.0 nM	0.51	0.86	1.13	1.31
	0.5 nM	0.51	0.71	0.85	0.38

<sup>a</sup>Chou-Talalay determination of drug synergy between **9** and vinblastine under light conditions ( $t_{\text{irr}} = 20$  min,  $\lambda_{\text{irr}} = 460\text{--}470$  nm, **56 J/cm**<sup>2</sup>). Effects on cell killing were determined by MTT 48 h after light treatment. Values shown in colored boxes denote combination indices (CI). CI > 1: antagonism, CI = 1: additive effect, CI < 1: synergy. CI values were obtained using Compusyn software.

## Conclusion

This is the first report on the synthesis and biological evaluation of metal-based inhibitors of the major human drug metabolizing enzyme CYP3A4. Using two analogs of ritonavir, we synthesized and characterized five Ru(II)-caged CYP3A4 inhibitors (**7 – 11**) that showed either single action PCT or dual action PCT/PDT behavior. Serendipitously, we demonstrated that CYP inhibition can be enhanced through inhibitor metalation, as the caged complexes can tightly and selectively bind to the CYP3A4 active site without heme ligation. Moreover, compound **9** was identified as a dual-action PCT/PDT lead compound, which effectively generates  ${}^1\text{O}_2$  and releases the CYP3A4

inhibitor to act synergistically with the common chemotherapeutic drug vinblastine in DU-145 adenocarcinoma cells. These findings warrant further studies on photoactive CYP inhibitory compounds to determine their potential use for clinical applications, such as enhancement of therapeutic efficacy of chemotherapeutic drugs.

**Acknowledgements.** This work was supported by the National Institutes of Health grants EB016072 (J.J.K. and C.T.) and ES025767 (I.F.S). C.T. and J.J.K. also thank the National Science Foundation (CHE 1800395), The Ohio State University and Wayne State University for partial support of this work. For instrumentation support we thank the NSF (0840413) and Penrose TherapeuTx. This work involves research carried out at the Stanford Synchrotron Radiation Lightsource. Use of the Stanford Synchrotron Radiation Lightsource, SLAC National Accelerator Laboratory, is supported by the U.S. Department of Energy, Office of Science, Office of Basic Energy Sciences under Contract No. DE-AC02-76SF00515. The SSRL Structural Molecular Biology Program is supported by the DOE Office of Biological and Environmental Research, and by the National Institutes of Health, National Institute of General Medical Sciences (P30GM133894).

## **Supporting Information**

The following information is available free of charge on the internet: Spectral data for **4**, **6-11**, inhibitory assays for other compounds, structural and cell viability data, **7-11** stability studies.

## Experimental Section

### Materials

**General Procedure for Synthesis of Ru(II) Complexes.** Some reactions were performed under ambient atmosphere unless otherwise noted. Anaerobic reactions were performed by purging the reaction solutions with Ar or nitrogen. Complexes **12** and **13** were purchased (Strem Chemicals). Complexes **14**,<sup>84</sup> **15**,<sup>85</sup> **16**,<sup>86</sup> **17**,<sup>86</sup> **18**,<sup>87</sup> **19**,<sup>88</sup> **20 – 22**,<sup>89</sup> **23 – 24**,<sup>90</sup> **25**,<sup>70</sup> and **26**<sup>91</sup> were prepared following literature protocols. For synthesis of **7 – 11**, a solution of [Ru(tpy)(L<sub>1</sub>)Cl]Cl in EtOH was treated with pyridine. Water was added and the mixture was deoxygenated by bubbling Ar through a submerged needle for 20 min. The pressure tube was sealed and heated to 80 °C for 16 h. The reaction mixture was cooled to room temperature, concentrated, and the residue was purified by column chromatography on neutral alumina to give [Ru(tpy)(L<sub>1</sub>)(L<sub>2</sub>)](Cl)<sub>2</sub> complexes.

**Synthesis of [Ru(tpy)(Me<sub>2</sub>bpy)(4)]Cl<sub>2</sub> (7).** [Ru(tpy)(Me<sub>2</sub>bpy)Cl]Cl<sup>67</sup> (19.0 mg, 0.0300 mmol) was added to a solution of **4** (28 mg, 0.070 mmol) in a 1:1 mixture of EtOH and H<sub>2</sub>O (3.0 mL each) under inert atmosphere in a pressure flask. The pressure flask was wrapped with aluminum foil. The solution was purged with argon for 10 min at room temperature. The pressure flask was sealed, and the reaction mixture refluxed at 80 °C for 16 h under an inert atmosphere. The color of the reaction mixture turned from purple to brown. The reaction mixture was cooled to room temperature and concentrated under reduced pressure. The crude product was purified over neutral alumina (5% MeOH/DCM) in the dark to give **7** as a brown solid (25 mg, 75%): <sup>1</sup>H NMR (400 MHz CD<sub>3</sub>OD) δ 8.75–8.72 (m, 1H), 8.69 (d, 2H, *J* = 8.4 Hz), 8.63 (d, 2H, *J* = 8.0 Hz), 8.48–8.45 (m, 1H), 8.29 (t, 1H, *J* = 8.0 Hz), 8.24–8.18 (m, 3H), 8.14 (t, 2H, *J* = 8.0 Hz), 7.81–7.72 (m, 2H), 7.66–7.60 (m, 4H), 7.55 (d, 1H, *J* = 5.6 Hz), 7.28–7.17 (m, 5H), 7.08 (t, 1H, *J* = 7.6 Hz), 7.01 (d, 1H, *J* = 7.6 Hz), 4.04–3.93 (m, 2H), 3.86–3.79 (m, 1H), 2.94–2.88 (m, 1H), 2.72 (t, 2H, *J* = 7.2

Hz), 2.68–2.65 (m, 1H), 2.60–2.55 (m, 2H), 2.34 (t, 2H,  $J$  = 7.2 Hz), 2.03 (s, 3H), 1.50 (s, 3H), 1.36–1.29 (m, 9H); IR  $\nu_{\text{max}}$  (cm<sup>-1</sup>) 3372, 2926, 2830, 1740, 1711, 1536, 1447, 1371, 1223, 1022, 519; ESMS calcd for C<sub>50</sub>H<sub>54</sub>N<sub>8</sub>O<sub>3</sub>RuS (M<sup>+</sup>) 474, found 474; UV-vis  $\lambda_{\text{max}}$  = 474 nm ( $\epsilon$  = 7700 M<sup>-1</sup>cm<sup>-1</sup>).

**Synthesis of [Ru(tpy)(Me<sub>2</sub>bpy)(6)]Cl<sub>2</sub> (8).** Compound **8** was prepared by following the general procedure by treating [Ru(tpy)(Me<sub>2</sub>bpy)Cl]Cl<sup>67</sup> (13 mg, 0.022 mmol) with **6** (23 mg, 0.044 mmol) in EtOH (3 ml) and water (3 ml). The residue was purified by column chromatography on neutral alumina (4-6% MeOH in DCM) to give red solid (15 mg, 63%). <sup>1</sup>H NMR (400 MHz, Methanol-*d*<sub>4</sub>)  $\delta$  8.76 (d,  $J$  = 8.0 Hz, 1H), 8.73 – 8.62 (m, 3H), 8.57 (t,  $J$  = 7.3 Hz, 1H), 8.50 (d,  $J$  = 8.1 Hz, 1H), 8.27 (dd,  $J$  = 9.2, 6.9 Hz, 3H), 8.18 (ddd,  $J$  = 12.3, 6.1, 3.6 Hz, 2H), 8.07 (ddt,  $J$  = 7.9, 3.9, 2.0 Hz, 1H), 7.77 (dt,  $J$  = 13.1, 7.7 Hz, 2H), 7.68 – 7.60 (m, 1H), 7.60 – 7.54 (m, 1H), 7.48 (dq,  $J$  = 8.7, 6.0, 4.8 Hz, 3H), 7.28 – 7.15 (m, 8H), 7.15 – 6.99 (m, 4H), 3.82 (ttd,  $J$  = 8.9, 6.7, 3.0 Hz, 1H), 3.55 (dd,  $J$  = 9.7, 5.7 Hz, 1H), 3.08 (ddd,  $J$  = 13.7, 9.7, 6.6 Hz, 1H), 2.97 – 2.81 (m, 2H), 2.78 – 2.60 (m, 5H), 2.10 (t,  $J$  = 8.1 Hz, 5H), 1.51 (d,  $J$  = 3.1 Hz, 3H), 1.39 – 1.25 (m, 9H), 1.25 – 1.18 (m, 2H); IR (KBr) 3395, 3242, 3058, 3027, 2974, 2927, 2859, 1698, 1660, 1602, 1542, 1523, 1496, 1447, 1388, 1364, 1282, 1248, 1168, 1119, 1078, 1016, 916, 778, 748, 701, 672, 646; UV-Vis:  $\lambda_{\text{max}}$  470 nm ( $\epsilon$  = 9,700 M<sup>-1</sup>cm<sup>-1</sup>); ESMS Calculated for C<sub>58</sub>H<sub>62</sub>N<sub>8</sub>O<sub>3</sub>RuS [M<sup>2+</sup>] 526, found 526.

**Synthesis of [Ru(tpy)(Me<sub>2</sub>dppn)(4)]Cl<sub>2</sub> (9).** Compound **9** was prepared by following the general procedure by treating [Ru(tpy)(Me<sub>2</sub>dppn)Cl]Cl<sup>65</sup> (22 mg, 0.029 mmol) with **4** (25 mg, 0.058 mmol) in EtOH (4 ml) and water (4 ml). The residue was purified by column chromatography on neutral alumina (3-4% MeOH in DCM) to give red solid (20 mg, 57%). <sup>1</sup>H NMR (400 MHz, Methanol-*d*<sub>4</sub>)  $\delta$  9.93 (dd,  $J$  = 8.4, 1.6 Hz, 1H), 9.33 (d,  $J$  = 8.2 Hz, 1H), 8.98 (d,  $J$  = 12.1 Hz, 2H), 8.78 (d,  $J$  = 8.1 Hz, 1H), 8.78 – 8.68 (m, 2H), 8.65 (d,  $J$  = 8.2 Hz, 1H), 8.33 – 8.23 (m, 3H), 8.26 – 8.17 (m,

1H), 8.16 (t,  $J$  = 7.8 Hz, 2H), 8.11 (h,  $J$  = 3.8 Hz, 2H), 7.75 – 7.68 (m, 2H), 7.68 – 7.58 (m, 3H), 7.61 – 7.50 (m, 1H), 7.50 (t,  $J$  = 6.7 Hz, 1H), 7.42 (d,  $J$  = 8.3 Hz, 1H), 7.26 – 7.09 (m, 7H), 4.03 (d,  $J$  = 4.6 Hz, 2H), 3.85 – 3.74 (m, 1H), 3.34 (d,  $J$  = 3.6 Hz, 1H), 2.86 (ddd,  $J$  = 15.9, 10.9, 5.5 Hz, 1H), 2.74 (t,  $J$  = 7.1 Hz, 2H), 2.66 – 2.58 (m, 1H), 2.58 (q,  $J$  = 2.7, 2.3 Hz, 2H), 2.37 (t,  $J$  = 7.0 Hz, 2H), 2.34 (s, 3H), 1.79 (s, 3H), 1.31 (d,  $J$  = 7.6 Hz, 9H); IR (KBr) 3394, 3056, 3027, 2924, 2853, 1966, 1697, 1662, 1542, 1520, 1446, 1363, 1247, 1167, 1056, 1017, 880, 776, 703; UV-Vis:  $\lambda_{\text{max}}$  485 nm ( $\mathcal{E}$  = 13,500 M<sup>-1</sup>cm<sup>-1</sup>); ESMS Calculated for C<sub>62</sub>H<sub>58</sub>ClN<sub>10</sub>O<sub>3</sub>RuS [M<sup>+</sup>] 1159, found 1159.

**Synthesis of [Ru(tpy)(Me<sub>2</sub>dppn)(6)]Cl<sub>2</sub> (10).** Compound **10** was prepared by following the general procedure by treating [Ru(tpy)(Me<sub>2</sub>dppn)Cl]Cl<sup>65</sup> (17 mg, 0.022 mmol) with **6** (23 mg, 0.044 mmol) in EtOH (5 ml) and water (5 ml). The residue was purified by column chromatography on neutral alumina (3-4% MeOH in DCM) to give red solid (17 mg, 61%). <sup>1</sup>H NMR (400 MHz, Methanol-*d*<sub>4</sub>)  $\delta$  9.96 (dd,  $J$  = 8.3, 6.4 Hz, 1H), 9.45 (dd,  $J$  = 8.2, 3.8 Hz, 1H), 9.14 – 9.02 (m, 2H), 8.83 – 8.72 (m, 2H), 8.68 (d,  $J$  = 8.0 Hz, 1H), 8.59 – 8.50 (m, 1H), 8.35 (t,  $J$  = 6.3 Hz, 1H), 8.26 (dtd,  $J$  = 15.0, 9.2, 5.4 Hz, 4H), 8.15 (dd,  $J$  = 18.4, 6.0 Hz, 2H), 8.05 – 7.98 (m, 1H), 7.77 – 7.66 (m, 3H), 7.61 – 7.53 (m, 3H), 7.57 – 7.30 (m, 2H), 7.18 (s, 4H), 7.27 – 7.12 (m, 1H), 7.16 – 7.04 (m, 5H), 3.76 – 3.46 (m, 1H), 3.47 (dt,  $J$  = 9.1, 6.0 Hz, 1H), 3.13 – 2.98 (m, 1H), 2.80 (dtd,  $J$  = 43.5, 15.3, 6.5 Hz, 1H), 2.67 (s, 2H), 2.67 – 2.58 (m, 1H), 2.56 (s, 1H), 2.36 (dd,  $J$  = 11.6, 3.3 Hz, 3H), 2.16 (dp,  $J$  = 21.1, 7.0 Hz, 1H), 1.80 (s, 3H), 1.29 (d,  $J$  = 8.1 Hz, 11H); IR (KBr) 3365, 3256, 3056, 3025, 2974, 2922, 2852, 2360, 2342, 1868, 1792, 1760, 1733, 1698, 1653, 1558, 1542, 1522, 1447, 1388, 1362, 1243, 1161, 1056, 881, 841, 775, 752, 700, 669; UV-Vis:  $\lambda_{\text{max}}$  480 nm ( $\mathcal{E}$  = 12,000 M<sup>-1</sup>cm<sup>-1</sup>); ESMS Calculated for C<sub>70</sub>H<sub>66</sub>ClN<sub>10</sub>O<sub>3</sub>RuS [M<sup>+</sup>] 1263, found 1263.

**Synthesis of  $[\text{Ru}(\text{tpy})(\text{Ph}_2\text{Me}_2\text{dppn})(\mathbf{4})]\text{Cl}_2$  (11).** Compound **11** was prepared by following the general procedure by treating  $[\text{Ru}(\text{tpy})(\text{Ph}_2\text{Me}_2\text{dppn})\text{Cl}]\text{Cl}^{68}$  (19 mg, 0.021 mmol) with **6** (22 mg, 0.042 mmol) in EtOH (3 ml) and water (3 ml). The residue was purified by column chromatography on neutral alumina (3-4% MeOH in DCM) to give red solid (14 mg, 48%).  $^1\text{H}$  NMR (400 MHz, Methanol-*d*<sub>4</sub>)  $\delta$  9.42 – 9.30 (m, 1H), 8.88 – 8.58 (m, 4H), 8.50 (dt, *J* = 6.6, 3.3 Hz, 1H), 8.32 – 7.89 (m, 9H), 7.83 – 7.55 (m, 14H), 7.46 – 7.29 (m, 2H), 7.29 – 6.96 (m, 12H), 3.83 – 3.68 (m, 1H), 3.46 (td, *J* = 9.2, 6.7 Hz, 1H), 2.99 (dd, *J* = 13.7, 9.6 Hz, 1H), 2.93 – 2.47 (m, 7H), 2.28 (d, *J* = 10.6 Hz, 3H), 2.14 (tdd, *J* = 16.6, 8.0, 3.7 Hz, 2H), 1.73 (s, 3H), 1.33 (d, *J* = 4.0 Hz, 1H), 1.27 (d, *J* = 2.2 Hz, 10H); IR (KBr) 3255, 3057, 3025, 2973, 2924, 2853, 2360, 2330, 1698, 1684, 1653, 1558, 1542, 1522, 1496, 1490, 1448, 1420, 1387, 1362, 1246, 1166, 1073, 1014, 839, 773, 701, 670; UV-Vis:  $\lambda_{\text{max}}$  491 nm ( $\mathcal{E}$  = 13,500 M<sup>-1</sup>cm<sup>-1</sup>); ESMS Calculated for  $\text{C}_{82}\text{H}_{74}\text{ClN}_{10}\text{O}_3\text{RuS}$  [M<sup>+</sup>] 1415, found 1415.

**Instrumentation and Methods.** NMR spectra were recorded on a Varian FT-NMR Mercury-400 MHz spectrometer. UV-Vis spectra were recorded on a Varian Cary 60 spectrophotometer. Steady state electronic absorption spectra were collected using an Agilent Cary 8453 diode array spectrometer and emission data were collected using a Horiba FluoroMax-4 fluorimeter. All experiments involving DU-145 cells were carried out in Dulbecco's modified Eagle's medium containing 10% FBS and 1000 units/mL penicillin/streptomycin. The irradiation source for quantum yield measurements was a 150 W Xe arc lamp (USHIO) in a MilliArc lamp housing unit, powered by an LPS-220 power supply and an LPS-221 igniter (PTI). The emission wavelengths were selected using a CVI Melles Griot long-pass filter and the appropriate irradiation wavelengths for photolysis experiments were selected with a bandpass filter (Thorlabs) and long-pass filter

(CVI Melles Griot). The quantum yields ( $\Phi$ ) for ligand dissociation were determined in CH<sub>3</sub>CN with an irradiation wavelength of 500 nm. The rate of moles reacted at early irradiation times was determined by monitoring the decrease in the MLCT absorption maximum as a function of time. The photon flux of the lamp with a 435 nm long-pass filter and a 500 nm bandpass filter was determined using ferrioxalate actinometry as previously described in detail.<sup>92</sup> Singlet oxygen quantum yields were performed using [Ru(bpy)<sub>3</sub>]<sup>2+</sup> as a standard ( $\Phi_{\Delta} = 0.81$  in MeOH), 1,3-diphenylisobenzofuran (DPBF) as a <sup>1</sup>O<sub>2</sub> trapping agent, and following a previously established procedure.<sup>93</sup>

**Studies on recombinant CYP3A4.** Full-length and truncated ( $\Delta$ 3-22) human CYP3A4 was expressed and purified as described previously.<sup>94</sup>

*Spectral Binding Titrations* – Equilibrium ligand binding to  $\Delta$ 3-22 CYP3A4 was monitored in a Cary 300 spectrophotometer at ambient temperature in 0.1 M phosphate buffer, pH 7.4, supplemented with 20% glycerol and 1 mM dithiothreitol. Inhibitors and caged compounds, with or without visible light irradiation ( $\lambda_{\text{irr}} = 400$ –700 nm,  $t_{\text{irr}} = 40$  min), were dissolved in DMSO and added to a 2  $\mu$ M protein solution in small aliquots, with the final solvent concentration <2%. Spectral dissociation constants ( $K_d$ ) were determined from hyperbolic fits to titration plots.

*Inhibitory Potency Assays* – Inhibitory potency for the 7-benzyloxy-4-(trifluoromethyl)coumarin (BFC) O-debenzylase activity of CYP3A4 was evaluated fluorometrically in a soluble reconstituted system. Full-length CYP3A4 and rat cytochrome P450 reductase (40  $\mu$ M and 60  $\mu$ M, respectively) were preincubated at room temperature for 1 h before 10-fold dilution with the reaction buffer consisting of 0.1 M potassium phosphate, pH 7.4, catalase and superoxide dismutase (2 Units/ml each). Prior to measurements, 85  $\mu$ l of the reaction buffer was mixed with 10  $\mu$ l of the NADPH-regenerating system (10 mM glucose, 0.2 mM NADP<sup>+</sup>, and 2 Units/ml

glucose-6-phosphate dehydrogenase), 5  $\mu$ l of the protein mixture (0.2  $\mu$ M final CYP3A4 concentration), and 2  $\mu$ l of the cage/inhibitor solution or DMSO. The mixture was incubated for 2 min, after which 1  $\mu$ l of 2 mM BFC and 1  $\mu$ l of 7 mM NADPH were added to initiate the reaction. Accumulation of the fluorescent product, 7-hydroxy-4-(trifluoromethyl)coumarin, was monitored for 2 min at room temperature in a Hitachi F400 fluorimeter ( $\lambda_{\text{ex}} = 404$  nm;  $\lambda_{\text{em}} = 500$  nm). Within this time interval, fluorescence changes were linear. The average of three measurements was used to calculate the remaining activity, with the DMSO-containing sample used as a control (100% activity). The  $\text{IC}_{50}$  values were derived from four-parameter logistic fittings to the [% activity] vs. [inhibitor] plots.

*Crystallization of 7- and 8-bound CYP3A4* - Both complexes were crystallized using a microbatch method under oil. Prior to crystallization setup,  $\Delta$ 3-22 CYP3A4 (50-60 mg/ml in 75-100 mM phosphate, pH 7.4) was incubated with a 2-fold ligand excess for 15 min and centrifuged to remove the precipitate. The supernatant (0.4  $\mu$ l) was mixed with 0.4-0.5  $\mu$ l of the crystallization solution containing: 10% PEG 3350 and 80 mM tribasic ammonium citrate, pH 7.0, for **7**, and 8% PEG 3350 and 70 mM DL-malate, pH 7.0, for **8**. Crystals were grown at room temperature for 2-3 days and cryoprotected with Paratone-N before freezing in liquid nitrogen.

*Determination of the X-ray structures* - X-ray diffraction data were collected at the Stanford Synchrotron Radiation Lightsource beamlines 9-2 and 12-2. Crystal structures were solved by molecular replacement with PHASER<sup>95</sup> and 5VCC as a search model. Ligands were built with eLBOW<sup>96</sup> and manually fit into the density with COOT.<sup>97</sup> The initial models were rebuilt and refined with COOT and PHENIX.<sup>96</sup> Polder omit electron density maps were calculated with PHENIX. Data collection and refinement statistics are summarized in Table S1. The atomic coordinates and structure factors for the **7**- and **8**-bound CYP3A4 were deposited to the Protein

Data Bank with the ID codes 7KS8 and 7KSA respectively.

**IC<sub>50</sub> Determination Studies** - Cytochrome P450 Inhibitor screening kits for CYP3A4, CYP1A2, and CYP2C9 were obtained from BioVision. Stock solutions of compounds **4**, **7**, and **9** were prepared at 5x concentrations in the provided assay buffer. Stock solutions were dispensed into triplicate wells of a 96-well plate and irradiated ( $t_{\text{irr}} = 20$  min,  $\lambda_{\text{irr}} = 460\text{--}470$  nm) or left in the dark. Compounds **4** and **7** (100  $\mu\text{M}$  to 100 nM) and compound **9** (100  $\mu\text{M}$  to 100 nM) were evaluated following the manufacturer's protocols. Percentage of enzyme activities was calculated from the initial linear slopes of the fluorescence vs. time plots (first 5 min), using solvent control (no inhibitor, 1% MeCN in assay buffer) as 100% activity. The slope of the blank plot (no enzyme, 1% MeCN in assay buffer) was subtracted from each experimental slope value. Percent inhibition was expressed as the quotient of the blank subtracted experimental slopes over the blank subtracted solvent control slope. Igor pro graphing software was used to produce % activity vs. Log (Molarity) dose response plots (Figure S15–S17), from which IC<sub>50</sub> values were determined.

**Biological Studies. General Viability Assays:** DU-145 cells were seeded in a 96-well plate at a density of 7000 cells per well in 100  $\mu\text{L}$  of Dulbecco's modified Eagle's medium (DMEM) containing 10% FBS and 1000 units/mL penicillin/streptomycin. Each plate was incubated in a 37 °C humidified incubator ventilated with 5% CO<sub>2</sub> overnight (16 h). The media was aspirated from each well, and octuplicate wells were treated with media containing **4** or **6–12** (5  $\mu\text{M}$ ) in DMEM media with 1% DMSO. Plates also contained blank wells with no cells and control wells with DMEM media containing 1% DMSO (vehicle). After 1 h of incubation at 37 °C, plates were removed from the incubator, the media was aspirated and replaced with either vehicle or media containing vinblastine (2.5–5 nM). The plates were then irradiated using a blue LED light source ( $t_{\text{irr}} = 20$  min,  $\lambda_{\text{irr}} = 460\text{--}470$  nm) or left in the dark and incubated for 72 h in a 37 °C humidified

incubator ventilated with 5% CO<sub>2</sub>. After incubation, MTT reagent (10 µL, 5 mg/mL in PBS) was added to each well, and plates were kept at 37 °C and 5% CO<sub>2</sub> for 2 h. The media was aspirated from each well, and DMSO (100 µL) was added. The wells were shaken for 30 min to allow solvation of the formazan crystals. Absorbance at 570 nm was measured in each well. Average absorbance values for the blank wells were subtracted from absorbance values for each sample to eliminate the background. Viability data were obtained by averaging blank-normalized absorbance values for control cells and expressing average absorbance for the treated samples as percent control.

*EC<sub>50</sub> Determination-* DU-145 human prostate cancer cells were seeded in a 96-well plate at a density of 7000 cells per well in 100 µL of Dulbecco's modified Eagle's medium (DMEM) containing 10% FBS and 1000 units/mL penicillin/streptomycin. Each plate was incubated in a 37 °C humidified incubator ventilated with 5% CO<sub>2</sub> overnight (16 h). The media was aspirated from each well, and quadruplicate wells were treated with media containing **4, 7, 9, 12** (25 µM–0.5 µM) or vinblastine (10 nM–0.5 nM) in 1% DMSO. Plates also contained blank wells with no cells and control wells with media containing 1% DMSO. After 1 h of incubation at 37 °C, wells containing **4, 7, 9, or 12** were aspirated and replaced with fresh media. Wells with vinblastine were left alone. Plates were then irradiated with blue light (460–470 nm; 20 min) or left in the dark and incubated for 72 h in a 37 °C humidified incubator ventilated with 5% CO<sub>2</sub>. After incubation, MTT reagent (10 µL, 5 mg/mL in PBS) was added to each well, and plates were kept at 37 °C and 5% CO<sub>2</sub> for 2 h. The media was aspirated from each well, and DMSO (100 µL) was added. The wells were shaken for 30 min to allow for the solvation of the formazan crystals. Absorbance at 570 nm was measured in each well. Average absorbance values for the blank wells were subtracted from absorbance values for each sample to eliminate the background. Viability data were obtained by

averaging normalized absorbance values for untreated cells and expressing absorbance for the treated samples as percent control. EC<sub>50</sub> values were determined using Igor Pro graphing software or Compusyn software.

*Chou-Talalay Synergy Determination-* DU-145 human prostate cancer cells were seeded in a 96-well plate at a density of 7000 cells per well in 100  $\mu$ L of Dulbecco's modified Eagle's medium (DMEM) containing 10% FBS and 1000 units/mL penicillin/streptomycin. Each plate was incubated in a 37 °C humidified incubator ventilated with 5% CO<sub>2</sub> overnight (16 h). The media was aspirated from each well and replaced with treatment media containing compound **9** (10  $\mu$ M–1  $\mu$ M) or vehicle (media with 1% DMSO). Plates were then incubated for 1 h. After incubation the media from each well was aspirated and replaced with media containing vinblastine (10 nM – 0.5 nM) or vehicle; resulting in vinblastine alone and **9** alone mono-treatments as well as combination treatments at each compound concentration, all in quadruplicate. Plates were then irradiated with blue light (460-470 nm; 20 min). After irradiation the plates were incubated in a 37 °C humidified incubator ventilated with 5% CO<sub>2</sub> for 72 h. After incubation, MTT reagent (10  $\mu$ L, 5 mg/mL in PBS) was added to each well, and plates were kept at 37 °C and 5% CO<sub>2</sub> for 2 h. The media was aspirated from each well, and DMSO (100  $\mu$ L) was added. The wells were shaken for 30 min to allow for the solvation of the formazan crystals. Absorbance at 570 nm was measured in each well. Average absorbance values for the blank wells were subtracted from absorbance values for each sample to eliminate the background. Viability data were obtained by averaging normalized absorbance values for untreated cells and expressing absorbance for the treated samples as percent effect. Dose and effect data points were then inserted into the Compusyn software, which solved for the EC<sub>50</sub> for both the mono-treatments and the combination as well as the CI values for each treatment combination (Figure 8).

## References

1. Chen, Q.; Wei, D., Human cytochrome P450 and personalized medicine. *Adv. Exp. Med. Biol.* **2015**, *827*, 341-51.
2. Guengerich, F. P.; Shimada, T., Oxidation of toxic and carcinogenic chemicals by human cytochrome P-450 enzymes. *Chem. Res. Toxicol.* **1991**, *4* (4), 391-407.
3. Li, A. P.; Kaminski, D. L.; Rasmussen, A., Substrates of human hepatic cytochrome P450 3A4. *Toxicology* **1995**, *104* (1-3), 1-8.
4. Guengerich, F. P., Cytochrome P-450 3A4: regulation and role in drug metabolism. *Annu. Rev. Pharmacol. Toxicol.* **1999**, *39*, 1-17.
5. Mehmood, Z.; Kelly, D. E.; Kelly, S. L., Cytochrome P450 3A4 mediated metabolism of 2,4-dichlorophenol. *Chemosphere* **1997**, *34* (11), 2281-2291.
6. Chae, Y. H.; Yun, C. H.; Guengerich, F. P.; Kadlubar, F. F.; el-Bayoumy, K., Roles of human hepatic and pulmonary cytochrome P450 enzymes in the metabolism of the environmental carcinogen 6-nitrochrysene. *Cancer. Res.* **1993**, *53* (9), 2028-2034.
7. Hodgson, E., In vitro human phase I metabolism of xenobiotics I: pesticides and related compounds used in agriculture and public health. *J. Biochem. Mol. Toxicol.* **2003**, *17* (4), 201-206.
8. Mehmood, Z.; Williamson, M. P.; Kelly, D. E.; Kelly, S. L., Human cytochrome P450 3A4 is involved in the biotransformation of the herbicide 2,4-dichlorophenoxyacetic acid. *Environ. Toxicol. Pharmacol.* **1996**, *2* (4), 397-401.
9. Mehmood, Z.; Williamson, M. P.; Kelly, D. E.; Kelly, S. L., Metabolism of organochlorine pesticides: the role of human cytochrome P450 3A4. *Chemosphere* **1996**, *33* (4), 759-769.
10. Xu, L.; Desai, M. C., Pharmacokinetic enhancers for HIV drugs. *Curr. Opin. Investig. Drugs* **2009**, *10* (8), 775-786.
11. Chapman, S. A.; Lake, K. D.; Solbrack, D. F.; Milfred, S. K.; Marshall, P. S.; Kamps, M. A., Considerations for using ketoconazole in solid organ transplant recipients receiving cyclosporine immunosuppression. *J. Transpl. Coord.* **1996**, *6* (3), 148-154.
12. Kempf, D. J.; Marsh, K. C.; Denissen, J. F.; McDonald, E.; Vasavanonda, S.; Flentge, C. A.; Green, B. E.; Fino, L.; Park, C. H.; Kong, X. P.; et al., ABT-538 is a potent inhibitor of human immunodeficiency virus protease and has high oral bioavailability in humans. *Proc. Natl. Acad. Sci.* **1995**, *92* (7), 2484-2488.
13. Brayer, S. W.; Reddy, K. R., Ritonavir-boosted protease inhibitor based therapy: a new strategy in chronic hepatitis C therapy. *Expert Rev. Gastroenterol. Hepatol.* **2015**, *9* (5), 547-558.
14. Kempf, D. J.; Marsh, K. C.; Kumar, G.; Rodrigues, A. D.; Denissen, J. F.; McDonald, E.; Kukulka, M. J.; Hsu, A.; Granneman, G. R.; Baroldi, P. A.; Sun, E.; Pizzuti, D.; Plattner, J. J.; Norbeck, D. W.; Leonard, J. M., Pharmacokinetic enhancement of inhibitors of the human immunodeficiency virus protease by coadministration with ritonavir. *Antimicrob. Agents Chemother.* **1997**, *41* (3), 654-660.
15. van Eijk, M.; Boosman, R. J.; Schinkel, A. H.; Huitema, A. D. R.; Beijnen, J. H., Cytochrome P450 3A4, 3A5, and 2C8 expression in breast, prostate, lung, endometrial, and ovarian tumors: relevance for resistance to taxanes. *Cancer Chemother. Pharmacol.* **2019**, *84* (3), 487-499.

16. Lolodi, O.; Wang, Y. M.; Wright, W. C.; Chen, T., Differential Regulation of CYP3A4 and CYP3A5 and its Implication in Drug Discovery. *Curr. Drug Metab.* **2017**, *18* (12), 1095-1105.

17. Thummel, K. E.; Wilkinson, G. R., In vitro and in vivo drug interactions involving human CYP3A. *Annu. Rev. Pharmacol. Toxicol.* **1998**, *38*, 389-430.

18. Teo, Y. L.; Ho, H. K.; Chan, A., Metabolism-related pharmacokinetic drug-drug interactions with tyrosine kinase inhibitors: current understanding, challenges and recommendations. *Br. J. Clin. Pharmacol.* **2015**, *79* (2), 241-53.

19. Breslin, S.; Lowry, M. C.; O'Driscoll, L., Neratinib resistance and cross-resistance to other HER2-targeted drugs due to increased activity of metabolism enzyme cytochrome P4503A4. *Br. J. Cancer* **2017**, *116* (5), 620-625.

20. Ikezoe, T.; Hisatake, Y.; Takeuchi, T.; Ohtsuki, Y.; Yang, Y.; Said, J. W.; Taguchi, H.; Koeffler, H. P., HIV-1 protease inhibitor, ritonavir: a potent inhibitor of CYP3A4, enhanced the anticancer effects of docetaxel in androgen-independent prostate cancer cells in vitro and in vivo. *Cancer Res* **2004**, *64* (20), 7426-31.

21. Martínez, C.; García-Martín, E.; Pizarro, R. M.; García-Gamito, F. J.; Agúndez, J. A. G., Expression of paclitaxel-inactivating CYP3A activity in human colorectal cancer: implications for drug therapy. *Br. J. Cancer* **2002**, *87* (6), 681-686.

22. Zamora, A.; Denning, C. A.; Heidary, D. K.; Wachter, E.; Nease, L. A.; Ruiz, J.; Glazer, E. C., Ruthenium-containing P450 inhibitors for dual enzyme inhibition and DNA damage. *Dalton Trans.* **2017**, *46* (7), 2165-2173.

23. Li, A.; Yadav, R.; White, J. K.; Herroon, M. K.; Callahan, B. P.; Podgorski, I.; Turro, C.; Scott, E. E.; Kodanko, J. J., Illuminating cytochrome P450 binding: Ru(II)-caged inhibitors of CYP17A1. *Chem. Commun.* **2017**, *53* (26), 3673-3676.

24. Karaoun, N.; Renfrew, A. K., A luminescent ruthenium(ii) complex for light-triggered drug release and live cell imaging. *Chem. Commun.* **2015**, *51* (74), 14038-14041.

25. White, J. K.; Schmehl, R. H.; Turro, C., An overview of photosubstitution reactions of Ru(II) imine complexes and their application in photobiology and photodynamic therapy. *Inorg. Chim. Acta* **2017**, *454*, 7-20.

26. Li, A.; Turro, C.; Kodanko, J. J., Ru(II) polypyridyl complexes as photocages for bioactive compounds containing nitriles and aromatic heterocycles. *Chem. Commun.* **2018**, *54*, 1280-1290.

27. Hopkins, S. L.; Bonnet, S. In *Ligand photosubstitution reactions with ruthenium compounds: applications in chemical biology and medicinal chemistry*, Wiley-VCH Verlag GmbH & Co. KGaA: 2017; pp 91-116.

28. Farrer, N. J.; Salassa, L.; Sadler, P. J., Photoactivated chemotherapy (PACT): the potential of excited-state d-block metals in medicine. *Dalton Trans.* **2009**, *(48)*, 10690-701.

29. Howerton, B. S.; Heidary, D. K.; Glazer, E. C., Strained ruthenium complexes are potent light-activated anticancer agents. *J. Am. Chem. Soc.* **2012**, *134* (20), 8324-8327.

30. Mari, C.; Pierroz, V.; Ferrari, S.; Gasser, G., Combination of Ru(II) complexes and light: new frontiers in cancer therapy. *Chem. Sci.* **2015**, *6* (5), 2660-2686.

31. van Rixel, V. H. S.; Ramu, V.; Auyeung, A. B.; Beztsinna, N.; Leger, D. Y.; Lameijer, L. N.; Hilt, S. T.; Le Devedec, S. E.; Yildiz, T.; Betancourt, T.; Gildner, M. B.; Hudnall, T. W.; Sol, V.; Liagre, B.; Kornienko, A.; Bonnet, S., Photo-Uncaging of a Microtubule-Targeted Rigidin Analogue in Hypoxic Cancer Cells and in a Xenograft Mouse Model. *J. Am. Chem. Soc.* **2019**, *141* (46), 18444-18454.

32. Puckett, C. A.; Ernst, R. J.; Barton, J. K., Exploring the cellular accumulation of metal complexes. *Dalton Trans.* **2010**, *39* (5), 1159-1170.

33. Puckett, C. A.; Barton, J. K., Mechanism of Cellular Uptake of a Ruthenium Polypyridyl Complex. *Biochemistry* **2008**, *47* (45), 11711-11716.

34. Mulcahy, S. P.; Li, S.; Korn, R.; Xie, X.; Meggers, E., Solid-phase synthesis of tris-heteroleptic ruthenium(II) complexes and application to acetylcholinesterase inhibition. *Inorg. Chem.* **2008**, *47* (12), 5030-5032.

35. Meggers, E., Targeting proteins with metal complexes. *Chem. Commun.* **2009**, (9), 1001-1010.

36. Respondek, T.; Sharma, R.; Herroon, M. K.; Garner, R. N.; Knoll, J. D.; Cueny, E.; Turro, C.; Podgorski, I.; Kodanko, J. J., Inhibition of Cathepsin Activity in a Cell-Based Assay by a Light-Activated Ruthenium Compound. *ChemMedChem* **2014**, *9*, 1306-1315.

37. Ramalho Suelem, D.; Vieira Paulo, C.; Sharma, R.; Kodanko Jeremy, J.; White Jessica, K.; Turro, C.; Aggarwal, N.; Chalasani, A.; Sameni, M.; Moin, K.; Sloane Bonnie, F.; Moin, K.; Sloane Bonnie, F., Imaging Sites of Inhibition of Proteolysis in Pathomimetic Human Breast Cancer Cultures by Light-Activated Ruthenium Compound. *PLoS One* **2015**, *10* (11), e0142527.

38. Hidayatullah, A. N.; Wachter, E.; Heidary, D. K.; Parkin, S.; Glazer, E. C., Photoactive Ru(II) Complexes With Dioxinophenanthroline Ligands Are Potent Cytotoxic Agents. *Inorg. Chem.* **2014**, *53* (19), 10030-10032.

39. Lee, J.; Udugamasooriya, D. G.; Lim, H.-S.; Kodadek, T., Potent and selective photo-inactivation of proteins with peptoid-ruthenium conjugates. *Nat. Chem. Biol.* **2010**, *6* (4), 258-260.

40. Allison, R. R.; Downie, G. H.; Cuenca, R.; Hu, X.-H.; Childs, C. J. H.; Sibata, C. H., Photosensitizers in clinical PDT. *Photodiagn. Photodyn. Ther.* **2004**, *1* (1), 27-42.

41. Smith, N. A.; Sadler, P. J., Photoactivatable metal complexes: from theory to applications in biotechnology and medicine. *Philos. Trans. R. Soc. A.* **2013**, *371* (1995), 20120519/1-20120519/13.

42. Schatzschneider, U., Photoactivated Biological Activity of Transition-Metal Complexes. *Eur. J. Inorg. Chem.* **2010**, (10), 1451-1467.

43. Frei, A.; Rubbiani, R.; Tubafard, S.; Blacque, O.; Anstaett, P.; Felgentrager, A.; Maisch, T.; Spiccia, L.; Gasser, G., Synthesis, Characterization, and Biological Evaluation of New Ru(II) Polypyridyl Photosensitizers for Photodynamic Therapy. *J. Med. Chem.* **2014**, *57* (17), 7280-7292.

44. Clarke, M. J., Ruthenium Metallopharmaceuticals. *Coord. Chem. Rev.* **2003**, *236* (1-2), 209-233.

45. Alessio, E.; Mestroni, G.; Bergamo, A.; Sava, G., Ruthenium anticancer drugs. *Met. Ions Biol. Syst.* **2004**, *42* (Metal Complexes in Tumor Diagnosis and as Anticancer Agents), 323-351.

46. Hartinger, C. G.; Zorbas-Seifried, S.; Jakupc, M. A.; Kynast, B.; Zorbas, H.; Keppler, B. K., From bench to bedside - preclinical and early clinical development of the anticancer agent indazolium trans-[tetrachlorobis(1H-indazole)ruthenate(III)] (KP1019 or FFC14A). *J. Inorg. Biochem.* **2006**, *100* (5-6), 891-904.

47. Alessio, E.; Mestroni, G.; Bergamo, A.; Sava, G., Ruthenium antimetastatic agents. *Curr. Top. Med. Chem.* **2004**, *4* (15), 1525-1535.

48. Arenas, Y.; Monro, S.; Shi, G.; Mandel, A.; McFarland, S.; Lilge, L., Photodynamic inactivation of *Staphylococcus aureus* and methicillin-resistant *Staphylococcus aureus* with Ru(II)-based type I/type II photosensitizers. *Photodiagn. Photodyn. Ther.* **2013**, *10* (4), 615-625.

49. Fong, J.; Kasimova, K.; Arenas, Y.; Kaspler, P.; Lazic, S.; Mandel, A.; Lilge, L., A novel class of ruthenium-based photosensitizers effectively kills in vitro cancer cells and in vivo tumors. *Photochem. Photobiol. Sci.* **2015**, *14* (11), 2014-2023.

50. Kaspler, P.; Lazic, S.; Forward, S.; Arenas, Y.; Mandel, A.; Lilge, L., A ruthenium(II) based photosensitizer and transferrin complexes enhance photo-physical properties, cell uptake, and photodynamic therapy safety and efficacy. *Photochem. Photobiol. Sci.* **2016**, *15* (4), 481-495.

51. Sevrioukova, I. F.; Poulos, T. L., Structure and mechanism of the complex between cytochrome P4503A4 and ritonavir. *Proc. Natl. Acad. Sci.* **2010**, *107* (43), 18422-18427.

52. Sevrioukova, I. F.; Poulos, T. L., Pyridine-Substituted Desoxyritonavir Is a More Potent Inhibitor of Cytochrome P450 3A4 than Ritonavir. *J. Med. Chem.* **2013**, *56* (9), 3733-3741.

53. Samuels, E. R.; Sevrioukova, I., Inhibition of Human CYP3A4 by Rationally Designed Ritonavir-Like Compounds: Impact and Interplay of the Side Group Functionalities. *Mol. Pharm.* **2018**, *15* (1), 279-288.

54. Rock, B. M.; Hengel, S. M.; Rock, D. A.; Wienkers, L. C.; Kunze, K. L., Characterization of Ritonavir-Mediated Inactivation of Cytochrome P450 3A4. *Mol. Pharmacol.* **2014**, *86* (6), 665.

55. Ekroos, M.; Sjögren, T., Structural basis for ligand promiscuity in cytochrome P450 3A4. *Proc. Natl. Acad. Sci.* **2006**, *103* (37), 13682.

56. Sevrioukova, I., Interaction of Human Drug-Metabolizing CYP3A4 with Small Inhibitory Molecules. *Biochemistry* **2019**, *58* (7), 930-939.

57. Kaur, P.; Chamberlin, A. R.; Poulos, T. L.; Sevrioukova, I. F., Structure-Based Inhibitor Design for Evaluation of a CYP3A4 Pharmacophore Model. *J. Med. Chem.* **2016**, *59* (9), 4210-4220.

58. Samuels, E. R.; Sevrioukova, I. F., An increase in side-group hydrophobicity largely improves the potency of ritonavir-like inhibitors of CYP3A4. *Biorg. Med. Chem.* **2020**, *28* (6), 115349.

59. Samuels, E. R.; Sevrioukova, I. F., Rational Design of CYP3A4 Inhibitors: A One-Atom Linker Elongation in Ritonavir-Like Compounds Leads to a Marked Improvement in the Binding Strength. *Int. J. Mol. Sci.* **2021**, *22* (2).

60. Knoll, J. D.; Albani, B. A.; Durr, C. B.; Turro, C., Unusually Efficient Pyridine Photodissociation from Ru(II) Complexes with Sterically Bulky Bidentate Ancillary Ligands. *J. Phys. Chem. A* **2014**, *118* (45), 10603-10610.

61. Loftus, L. M.; White, J. K.; Albani, B. A.; Kohler, L.; Kodanko, J. J.; Thummel, R. P.; Dunbar, K. R.; Turro, C., New RuII Complex for Dual Activity: Photoinduced Ligand Release and 1O2 Production. *Chem. Eur. J.* **2016**, *22* (11), 3704-3708.

62. Li, A.; White, J. K.; Arora, K.; Herroon, M. K.; Martin, P. D.; Schlegel, H. B.; Podgorski, I.; Turro, C.; Kodanko, J. J., Selective Release of Aromatic Heterocycles from Ruthenium Tris(2-pyridylmethyl)amine with Visible Light. *Inorg. Chem.* **2016**, *55* (1), 10-12.

63. Samuels, E. R.; Sevrioukova, I. F., Direct synthesis of  $\alpha$ -thio aromatic acids from aromatic amino acids. *Tetrahedron Lett.* **2018**, *59* (12), 1140-1142.

64. Huisman, M.; White, J. K.; Lewalski, V. G.; Podgorski, I.; Turro, C.; Kodanko, J. J., Caging the uncageable: using metal complex release for photochemical control over irreversible inhibition. *Chem. Commun.* **2016**, *52* (85), 12590-12593.

65. Arora, K.; Herroon, M.; Al-Afyouni, M. H.; Toupin, N. P.; Rohrbaugh, T. N.; Loftus, L. M.; Podgorski, I.; Turro, C.; Kodanko, J. J., Catch and Release Photosensitizers: Combining

Dual-Action Ruthenium Complexes with Protease Inactivation for Targeting Invasive Cancers. *J. Am. Chem. Soc.* **2018**, *140* (43), 14367-14380.

66. Bahreman, A.; Limburg, B.; Siegler, M. A.; Koning, R.; Koster, A. J.; Bonnet, S., Ruthenium Polypyridyl Complexes Hopping at Anionic Lipid Bilayers through a Supramolecular Bond Sensitive to Visible Light. *Chem. Eur. J.* **2012**, *18* (33), 10271-10280.

67. Bahreman, A.; Limburg, B.; Siegler, M. A.; Bouwman, E.; Bonnet, S., Spontaneous Formation in the Dark, and Visible Light-Induced Cleavage, of a Ru-S Bond in Water: A Thermodynamic and Kinetic Study. *Inorg. Chem.* **2013**, *52* (16), 9456-9469.

68. Toupin, N. P.; Nadella, S.; Steinke, S. J.; Turro, C.; Kodanko, J. J., Dual-Action Ru(II) Complexes with Bulky  $\pi$ -Expansive Ligands: Phototoxicity without DNA Intercalation. *Inorg. Chem.* **2020**, *59* (6), 3919-3933.

69. Knoll, J. D.; Albani, B. A.; Turro, C., New Ru(II) Complexes for Dual Photoreactivity: Ligand Exchange and  $^1\text{O}_2$  Generation. *Acc. Chem. Res.* **2015**, *48* (8), 2280-2287.

70. Knoll, J. D.; Albani, B. A.; Turro, C., Excited state investigation of a new Ru(II) complex for dual reactivity with low energy light. *Chem. Commun.* **2015**, *51* (42), 8777-8780.

71. Albani, B. A.; Pena, B.; Leed, N. A.; de Paula, N. A. B. G.; Pavani, C.; Baptista, M. S.; Dunbar, K. R.; Turro, C., Marked Improvement in Photoinduced Cell Death by a New Tris-heteroleptic Complex with Dual Action: Singlet Oxygen Sensitization and Ligand Dissociation. *J. Am. Chem. Soc.* **2014**, *136* (49), 17095-17101.

72. Rohrbaugh, T. N., Jr.; Rohrbaugh, A. M.; Kodanko, J. J.; White, J. K.; Turro, C., Photoactivation of imatinib-antibody conjugate using low-energy visible light from Ru(II)-polypyridyl cages. *Chem. Commun.* **2018**, *54* (41), 5193-5196.

73. Li, A.; Yadav, R.; White, J. K.; Herroon, M. K.; Callahan, B. P.; Podgorski, I.; Turro, C.; Scott, E. E.; Kodanko, J. J., Illuminating cytochrome P450 binding: Ru (II)-caged inhibitors of CYP17A1. *Chem. Commun.* **2017**, *53* (26), 3673-3676.

74. Li, A.; White, J. K.; Arora, K.; Herroon, M. K.; Martin, P. D.; Schlegel, H. B.; Podgorski, I.; Turro, C.; Kodanko, J. J., Selective Release of Aromatic Heterocycles from Ruthenium Tris (2-pyridylmethyl) amine with Visible Light. *Inorg. Chem.* **2015**, *55* (1), 10-12.

75. Feng, B. Y.; Shoichet, B. K., A detergent-based assay for the detection of promiscuous inhibitors. *Nat. Protoc.* **2006**, *1* (2), 550-553.

76. Paine, M. F.; Hart, H. L.; Ludington, S. S.; Haining, R. L.; Rettie, A. E.; Zeldin, D. C., The human intestinal cytochrome P450 "pie". *Drug Metab. Dispos.* **2006**, *34* (5), 880-886.

77. Blagosklonny, M. V.; Dixon, S. C.; Figg, W. D., Efficacy of microtubule-active drugs followed by ketoconazole in human metastatic prostate cancer cell lines. *J. Urol.* **2000**, *163* (3), 1022-1026.

78. Ikezoe, T.; Hisatake, Y.; Takeuchi, T.; Ohtsuki, Y.; Yang, Y.; Said, J. W.; Taguchi, H.; Koeffler, H. P., HIV-1 Protease Inhibitor, RitonavirA Potent Inhibitor of CYP3A4, Enhanced the Anticancer Effects of Docetaxel in Androgen-Independent Prostate Cancer Cells In vitro and In vivo. *Cancer Res.* **2004**, *64* (20), 7426.

79. Zhong, D.; Wu, H.; Wu, Y.; Li, Y.; Yang, J.; Gong, Q.; Luo, K.; Gu, Z., Redox dual-responsive dendrimeric nanoparticles for mutually synergistic chemo-photodynamic therapy to overcome drug resistance. *J. Control. Release* **2020**.

80. Chou, T.-C., Drug Combination Studies and Their Synergy Quantification Using the Chou-Talalay Method. *Cancer Res.* **2010**, *70* (2), 440-446.

81. Diana Duarte, N. V., New Trends for Antimalarial Drugs: Synergism between Antineoplastics and Antimalarials on Breast Cancer Cells. *Biomolecules* **2020**, *10*, 1623.

82. Jean-Nicolas Gallant, J. E. A., Charles D. Smith, David T. Dicker, Wenge Wang, Nathan G. Dolloff, Arunasalam Navaraj & Wafik S. El-Deiry, Quinacrine synergizes with 5-fluorouracil and other therapies in colorectal cancer. *Canc. Biol. Ther.* **2011**, *12* (3), 239-251.

83. Ru-pin Alicia Chi, P. v. d. W., Wei Wei, Michael J. Birrer and Virna D. Leaner, Inhibition of Kpn $\beta$ 1 mediated nuclear import enhances cisplatin chemosensitivity in cervical cancer. *BMC Cancer* **2021**, *21* (106), 1-16.

84. Bomben, P. G.; Robson, K. C. D.; Sedach, P. A.; Berlinguette, C. P., On the Viability of Cyclometalated Ru(II) Complexes for Light-Harvesting Applications. *Inorg. Chem.* **2009**, *48* (20), 9631-9643.

85. Thomas, R. A.; Tsai, C. N.; Mazumder, S.; Lu, I. C.; Lord, R. L.; Schlegel, H. B.; Chen, Y. J.; Endicott, J. F., Energy Dependence of the Ruthenium(II)-Bipyridine Metal-to-Ligand-Charge-Transfer Excited State Radiative Lifetimes: Effects of  $\pi\pi^*$ (bipyridine) Mixing. *J. Phys. Chem. B* **2015**, *119* (24), 7393-7406.

86. Garner, R. N.; Joyce, L. E.; Turro, C., Effect of electronic structure on the photoinduced ligand exchange of Ru(II) polypyridine complexes. *Inorg. Chem.* **2011**, *50* (10), 4384-4391.

87. McConnell, A. J.; Lim, M. H.; Olmon, E. D.; Song, H.; Dervan, E. E.; Barton, J. K., Luminescent Properties of Ruthenium(II) Complexes with Sterically Expansive Ligands Bound to DNA Defects. *Inorg. Chem.* **2012**, *51* (22), 12511-12520.

88. Pena, B.; Leed, N. A.; Dunbar, K. R.; Turro, C., Excited state dynamics of two new Ru(II) cyclometallated dyes: relation to cells for solar energy conversion and comparison to conventional systems. *J. Phys. Chem. C* **2012**, *116* (42), 22186-22195.

89. Habtemariam, A.; Melchart, M.; Fernández, R.; Parsons, S.; Oswald, I. D. H.; Parkin, A.; Fabbiani, F. P. A.; Davidson, J. E.; Dawson, A.; Aird, R. E.; Jodrell, D. I.; Sadler, P. J., Structure-Activity Relationships for Cytotoxic Ruthenium(II) Arene Complexes Containing N,N-, N,O-, and O,O-Chelating Ligands. *J. Med. Chem.* **2006**, *49* (23), 6858-6868.

90. Kender, W. T.; Turro, C., Unusually Slow Internal Conversion in N-Heterocyclic Carbene/Carbanion Cyclometallated Ru(II) Complexes: A Hammett Relationship. *J. Phys. Chem. A* **2019**, *123*, 2650-2660.

91. Dovletoglou, A.; Adeyemi, S. A.; Meyer, T. J., Coordination and Redox Chemistry of Substituted-Polypyridyl Complexes of Ruthenium. *Inorg. Chem.* **1996**, *35* (14), 4120-4127.

92. Montalti, M.; Credi, A.; Prodi, L.; Gandolfi, M. T., *Handbook of Photochemistry*. 3rd ed.; CRC Press: Boca Raton, FL, 2006.

93. Rohrbaugh, T. N., Jr.; Collins, K. A.; Xue, C.; White, J. K.; Kodanko, J. J.; Turro, C., New Ru(II) complex for dual phototherapy: release of cathepsin K inhibitor and 1O<sub>2</sub> production. *Dalton Trans.* **2018**, *47*, 11851-11858.

94. Sevrioukova, I. F., High-Level Production and Properties of the Cysteine-Depleted Cytochrome P450 3A4. *Biochemistry* **2017**, *56* (24), 3058-3067.

95. McCoy, A. J.; Grosse-Kunstleve, R. W.; Adams, P. D.; Winn, M. D.; Storoni, L. C.; Read, R. J., Phaser crystallographic software. *J. Appl. Crystallogr.* **2007**, *40* (4), 658-674.

96. Adams, P. D.; Afonine, P. V.; Bunkoczi, G.; Chen, V. B.; Davis, I. W.; Echols, N.; Headd, J. J.; Hung, L. W.; Kapral, G. J.; Grosse-Kunstleve, R. W.; McCoy, A. J.; Moriarty, N. W.; Oeffner, R.; Read, R. J.; Richardson, D. C.; Richardson, J. S.; Terwilliger, T. C.; Zwart, P. H., PHENIX: a comprehensive Python-based system for macromolecular structure solution. *Acta Crystallogr., Sect. D: Biol. Crystallogr.* **2010**, *66* (2), 213-221.

97. Emsley, P.; Lohkamp, B.; Scott, W. G.; Cowtan, K., Features and development of Coot. *Acta Crystallogr., Sect. D: Biol. Crystallogr.* **2010**, *66* (4), 486-501.



TOC Graphic

